Combustion and Flame 286 (2026) 114817

Contents lists available at ScienceDirect

Combustion and Flame

journal homepage: www.sciencedirect.com/journal/combustion-and-flame

Unravelling the unique kinetic interactions between N_2O and unsaturated hydrocarbons

Hongqing Wu [a,1], Guojie Liang [a,1], Tianzhou Jiang [a], Fan Li [b], Yang Li [d], Rongpei Jiang [e], Ruoyue Tang [a], Song Cheng [a,c,*]

[a] Department of Mechanical Engineering, The Hong Kong Polytechnic University, Kowloon, Hong Kong SAR 999077, China
[b] Department of Aeronautical and Aviation Engineering, The Hong Kong Polytechnic University, Kowloon, Hong Kong SAR 999077, China
[c] Research Institute for Smart Energy, The Hong Kong Polytechnic University, Kowloon, Hong Kong SAR 999077, China
[d] National Key Laboratory of Solid Propulsion, School of Astronautics, Northwestern Polytechnical University, Xi'an, China
[e] Beijing Institute of Aerospace Testing Technology, Beijing, China

ARTICLE INFO

Keywords:
Unsaturated hydrocarbons
N_2O
Kinetic interactions
Ab initio calculations
Kinetic modeling and validation

ABSTRACT

The interaction between unsaturated hydrocarbons and N_2O has attracted considerable attention in recent years due to their important role as potential propellants for advanced propulsion systems (e.g. Nitrous oxide fuel blend (NOFBX)) and key combustion intermediates in exhaust gas recirculation systems. Although experimental studies and kinetic models have been developed to investigate its fuel chemistry, discrepancies remain between modeled and measured ignition delay times at low temperatures. In this work, we characterize previously unreported direct interaction pathways between N_2O and unsaturated hydrocarbons (C_2H_4, C_3H_6, C_2H_2, C_3H_4-A, and C_3H_4-P) through quantum chemistry calculations, comprehensive kinetic modeling, and experimental validation. These reactions proceed via O-atom addition from N_2O to unsaturated hydrocarbons, forming five-membered ring intermediates that decompose into N_2 and hydrocarbon-specific products. Distinct differences are identified between alkenes and dienes and alkynes, arising from the disparity in N–C bond lengths within the intermediates (~1.480 Å for alkenes and 1.429 Å for dienes vs. ~1.381 Å for alkynes), which governs their decomposition pathways. The corresponding rate coefficients are determined and implemented into multiple kinetic models, with autoignition simulations showing a pronounced promoting effect on model reactivity and improved agreement with experiments, especially at low temperatures. Comprehensive uncertainty analyses of the potential energy surfaces, rate coefficients, and ignition delay times are conducted to ensure the robustness and reliability of the findings. Flux analysis further reveals that the new pathways suppress conventional inhibiting channels while enabling aldehyde- and ketone-forming pathways that enhance overall reactivity, with JSR simulations further confirming the feasibility of validating these pathways through experiments. This work provides a more complete description of N_2O–hydrocarbon interactions and reveals other important N_2O–hydrocarbon interaction chemistries that need to be further studied via both theoretical and experimental investigations.

1. Introduction

Nitrous oxide (N_2O), a major component of the NO_x family, is a reactive gas commonly produced during combustion processes [1]. It is stable and comparatively unreactive at room temperatures [2]. As a strong oxidant, it can sustain combustion even in the absence of molecular oxygen [3]. These benefits make N_2O an ideal candidate for rocket propulsion applications. On the other hand, unsaturated hydrocarbons containing double or triple bonds between adjacent carbon atoms are highly reactive and readily undergo addition reactions with elemental halogens, hydrogen halides, alcohols, and many other compounds [4–6]. They also serve as potential fuels or propellants for advanced propulsion systems and are key intermediate products in alkane oxidation [7].

The co-existence of N_2O and unsaturated hydrocarbons can be found in many applications. For instance, the need for high-performance

---

* Corresponding author.
E-mail address: songcheng@polyu.edu.hk (S. Cheng).
[1] Both authors contribute equally to this paper.

https://doi.org/10.1016/j.combustflame.2026.114817
Received 2 September 2025; Received in revised form 20 January 2026; Accepted 21 January 2026

propellants for advanced propulsion systems has pushed the development of new propellants based on N_2O and unsaturated hydrocarbons. In the past decades, hydrazine and hydrazine derivatives like monomethyl hydrazine (MMH) and unsymmetrical dimethyl hydrazine (DMH) are used for spacecraft propulsion applications due to their advantages of long term storable, easy to decompose via catalyst, low risk of unwanted decomposition or explosion, etc. [8,9]. However, these propellants are highly toxic and carcinogenic [10], resulting in high handling and transportation costs. In recent years, NOFBX (Nitrous Oxide Fuel Blend) has emerged as a promising alternative due to advantages including non-toxic nature, high performance, and low cost [11–13]. As a monopropellant, NOFBX is a mixture of unsaturated hydrocarbons (e.g. C_2H_2, C_3H_4-P, C_3H_4-A, C_2H_4, or C_3H_6) with nitrous oxide. On the other hand, exhaust gas recirculation (EGR) has also received significant attention due to its ability to mitigate NO_x formation and enhance system efficiency. Extensive research has been devoted to understanding the underlying fundamentals for EGR [14–17]. During EGR operation, the N_2O remaining in the exhaust gas can interact with the unsaturated hydrocarbons produced from fuel decomposition and oxidation, affecting global combustion and emission characteristics of the engine system. These applications make it necessary to understand the chemical kinetic interactions between unsaturated hydrocarbons and N_2O.

There have been only a few experimental studies on the combustion characteristics of unsaturated hydrocarbons with N_2O blending, as shown in Table 1. In the early 1960s, Trenwith [18] studied the oxidation of C_2H_4 by N_2O at temperatures of 555−602 °C and pressures of 20−100 mmHg. CH_3CHO was identified as a primary product from C_2H_4 and N_2O reactions, and global reaction rate constants were proposed for consumption of C_2H_4 by N_2O. More recently, Deng et al. [19] measured the ignition delay times of stoichiometric $C_2H_4/O_2/N_2O/Ar$ mixtures with molar blending ratios of $N_2O/(N_2O + O_2) = 0$, 50, 80, and 100 %. Experiments were conducted in a shock tube at pressures of 1.2−10 atm, fuel-equivalence ratios of 0.5−2.0, and temperatures of 1214−1817 K, from which it was found that the ignition delay times of C_2H_4 increase as the N_2O concentration increases at a given pressure and temperature. Naumann et al. [8] and Kick et al. [20] investigated the ignition delay times and laminar flame speeds of ethene/ nitrous oxide mixtures diluted with nitrogen, carbon dioxide, or Argon at pressures ranging from 1 to 16 bar and temperatures of 1000–2000 K using a shock tube and burner, respectively. Based on their experimental results, they modified several reactions within the nitrogen subsystem to improve the predictive capability of the publicly available GRI 3.0 mechanism. Zhang et al. [11] measured the ignition delay times of a N_2O-C_2H_4 NOFBX propellant using a rapid compression machine under T_C = 885–940 K, p_C = 2.5–4.3 MPa, and fuel-equivalence ratios of 1.05–1.35. Modeling was also conducted using existing chemistry models, where the results showed notable discrepancies between experimental measurements and model predictions at low temperatures, indicating the insufficiency in existing chemistry models for N_2O and C_2H_4 interactions.

Table 1
Experimental investigations for fundamental combustion characteristics of N_2O/C2 hydrocarbons blends.

Name	Experimental setup	Properties	Experimental conditions	Ref.
Trenwith	Cylindrical silica vessel	Speciation	C_2H_4/N_2O, T = 828–875 K, p = 20–100 mm	[18]
Deng	Shock tube	IDT	$C_2H_4/N_2O/Ar$, φ = 0.5–2.0, T = 1090–1760 K, p = 1.2–10 atm	[19]
Naumann	Shock tube	IDT	C_2H_4/N_2O: 20 %, N_2: 80 %, φ = 1.0, T = 1050–2000 K, p = 1, 4, 16 bar	[8]
	Burner	Laminar flame speed	C_2H_4/N_2O: 50 %, N_2: 50 %, T = 473 K, p = 1, 3, 6 and 10 bar	
Kick	Shock tube	IDT	$C_2H_4/N_2O/N_2/Ar/CO_2$, φ = 1.0, T = 1050–2000 K, p = 1, 4, 16 bar,	[20]
	Burner	Laminar flame speed	C_2H_4/N_2O: 50 %, N_2: 50 %, T = 473 K, p = 1, 3, and 6 bar	
Zhang	Rapid compression machine	IDT	$C_2H_4/N_2O/Ar$, φ = 1.05–1.35, N_2O: 40.8 %, 42.5 %, T = 885–940 K p = 2.5–4.3 MPa	[11]
Yang	Rapid compression machine	IDT	$C_2H_4/N_2O/Ar$, φ = 0.5–2, N_2O:1.5 %, 3 %, T = 1170–1290 K, p = 15–45 bar	[21]
Wang	Steel cube chamber	Flame speed	$C_2H_4/N_2O/Ar$, φ = 0.2–2.4, T = 280 K, p = 0.5–2.0 atm	[22]
Mevel	Shock tube	IDT	$C_2H_4/C_2H_2/O_2/N_2O/Ar$, φ = 0.78–1.80, T =1269–1945 K, p = 222–397 kPa	[23]
Darian	Burner	Speciation	C_2H_2/N_2O, P = 20–40 mmHg, φ = 0.5–1.8	[24]
Aldous	Bunsen burner	Flame speed	C_2H_2/N_2O, φ = 0.35–2.0, T = 400/500/600 K, p = 1 atm	[25]

Although the experimental observations reviewed above have shown strong kinetic interactions between N_2O and unsaturated hydrocarbons and existing chemistry models are continuously refined [26–28], theoretical studies of the interactive kinetics between unsaturated hydrocarbons and N_2O remain seriously limited. To date, there have been only a few *ab initio* studies on the interactions between C_2H_4 and N_2O, as well as between C_2H_2 and N_2O, as critically reviewed in [1]. For the C_2H_4 and N_2O system, Ess et al. and [29] Grimme et al. [30] investigated the potential energy surface (PES) governing the interaction between C_2H_4 and N_2O, leading to the formation of a $(CH_2)_2ON_2$ five-membered ring intermediate. In addition, Li. et al. [31] revealed a reaction pathway on the PES in which C_2H_4 reacts with N_2O to produce CH_3, CHO, and N_2. Parmon et al. [32] proposed that if the C=C bond is located at the terminal of an unsaturated hydrocarbon molecule, the O atom from N_2O can be added to either carbon atom of the double bond, yielding ketones or aldehydes depending on the O atom addition site. For the C_2H_2 and N_2O system, Ess et al. [29], Grimme et al. [30], and Liu et al. [33] explored the PES associated with the interaction between C_2H_2 and N_2O, resulting in the formation of a $(CH)_2ON_2$ five-membered ring intermediate. Furthermore, Karami et al. [34] investigated the reaction mechanism of C_2H_2 and N_2O leading to the formation of CH_2CO and N_2 on the singlet PES. Unfortunately, the existing studies on alkenes & dienes and N_2O did not determine any rate parameters. As such, the existing chemistry models for unsaturated hydrocarbon/N_2O systems currently do not include their direct interacting reactions. Although these reacting pathways can be important at low temperatures due to the low energy barrier for such addition reactions, their rate coefficients have not yet been reported in the literature. Previous research from the authors' group [35–37] have revealed important direct interacting reactions between NO_x and unsaturated hydrocarbons (e.g., RH + NO_2 pathways, $ROO^{\cdot}$ + NO pathways) where these reactions are found to greatly affect fuel reactivity. The current study serves as a continuation of this dedicated effort, with the aims to: (a) investigate the direct interacting pathways and, for the first time, their respective rate parameters between N_2O and C_2-C_3 alkenes, diene and alkynes (C_2H_4, C_3H_6, C_3H_4-A, C_2H_2, and C_3H_4-P); (b) elucidate the similarities and differences in direct interacting pathways steps between alkene/N_2O, diene/N_2O and alkyne/N_2O; and (c) systematically evaluate the impact of these reactions on chemical kinetic model performance predictions through kinetic modeling.

2. Computational methods

2.1. Potential energy surfaces

Electronic geometries, vibrational frequencies and zero-point energies for all species involved in the 6 reactions (including reactants, products, complexes, intermediates (INTs), transition states (TS's)) are calculated at the M06–2X method [38] coupled with the 6–311++G(d, p) basis set [39–42]. Following this, conformer search at the same level of theory is conducted to ensure the optimized structures retain the lowest energy. Intrinsic reaction coordinate (IRC) calculations are carried out at the same level of theory to ensure that the transition state connects the respective reactants with the respective product complex. 1-D hindered rotor treatment [43] are also obtained at the M06–2X/6–311++G(d, p) level of theory for the low frequency torsional modes between non-hydrogen atoms in all of the reactants, TS's, complexes, intermediates and products, with a total of 36 scans (i.e., 10 degrees increment in the respective dihedral angle) for each rotor. Vibrational frequencies obtained from *ab initio* methods rarely match their experimental counterparts, primarily due to the imperfect treatment of electron–electron interactions and the neglect of anharmonic effects [44]. These limitations also introduce systematic errors into the computed vibrational zero-point energies (ZPE) [38]. Consequently, scaling factors of 0.982 and 0.970 are applied to correct the calculated harmonic frequencies and ZPE, respectively. These factors were recommended by the developers of the M06–2X functional, i.e., Zhao and Truhlar [38]. Both scaling factors are typically derived from systematic studies of large datasets, where the discrepancies between computational and experimental results are analyzed and corrected. As a result, these factors are widely adopted to reduce systematic deviations between calculated values and experimental vibrational frequencies and ZPE. Single-point energies (SPEs) are further determined for all the species using the CCSD(T) method with the complete basis set limit (CBS) [45] extrapolated by cc-pVTZ and cc-pVQZ [46] as:

$$E_{CBS} = E_{CCSD(T)/cc-pVQZ} + \left(E_{CCSD(T)/cc-pVQZ} - E_{CCSD(T)/cc-pVTZ}\right) * \frac{4^4}{5^4 - 4^4} \quad (1)$$

With the CCSD(T) method, attention must be addressed to T1 diagnostic [47] to measure the multi-reference characteristics. Timothy et al. [48] has established that the T1 diagnostic component in the CCSD wavefunction reflects the significance of non-dynamical electron correlation by using localized and Brueckner-like orbitals, with a large value indicating that such correlation effects are important. A large T1 value for canonical RHF SCF (Restricted Hartree-Fock Self-Consistent Field) orbitals suggests the presence of important configurations in the n-particle space, which should be considered in a singles and doubles dynamical electron correlation procedure. If the T1 value exceeds 0.04, the calculation should consider the doubles dynamical electron correlation procedure [49]. The T1 diagnostic values for all the species, as summarized in Table S1 in the Supplementary Material, are below 0.033, which indicates that the SPEs calculated from using single-reference calculation method are reliable in this study. All the calculations mentioned above are performed using ORCA 5.0.4 [50] or GAUSSIAN [51], and the optimized structures for all species, TS's and complexes as well as the heats of formation of the reactants and products, are summarized in the Supplementary Material.

2.2. Rate coefficients calculations

The reaction rate coefficients, k, which quantify the temperature-dependent probability of a reaction occurring per unit concentration, are obtained using canonical transition state theory with hindered-rotor corrections. The Master Equation System Solver (MESS) program suite [52] is employed here to calculate the chemical rate coefficients for the reactions via solution of the one-dimensional master equation, based on the chemically significant eigenstate approach of Miller and Klippenstein [53] and the bimolecular species model of Georgievskii and Klippenstein [54]. The frequencies of lower-frequency modes are replaced by the hindered rotor potentials obtained from 1-D scans. Quantum mechanical tunneling corrections assuming the asymmetric Eckart potential (TST/Eck) [55] are applied to obtain the rate coefficient over the temperature range of 298–2000 K. To assess possible pressure effects, pressure-dependent rates are evaluated at 0.01, 0.1, 0.316, 1.0, 3.16, 10.0, 31.6, and 100 bar. As the reaction rate coefficients showed negligible differences within this pressure range, the 100 bar values are adopted in this study. All rate coefficients are fitted to the modified Arrhenius equation: $k = AT^n \exp(-E_a/RT)$.

2.3. Kinetic modeling

There are four chemical kinetic mechanisms suitable for predicting the IDTs of unsaturated hydrocarbon/N_2O mixtures: (1) the Aramco 3.0 [56] model, (2) the DLR SynNG + NO [10] model, (3) the GRI 3.0 [57] model, and (4) the NUIG 1.1 [58] model. The NO_X sub-mechanism (89 species, 765 reactions) describing reactions of NO_X and its interactions with C0–C2 species, developed by Glarborg et al. [59], are incorporated into all four mechanisms. In addition, the C1–C2 hydrocarbon sub-mechanisms developed by Hashemi et al. [60,61] and Gimenez-Lopez et al. [62] are included in Aramco 3.0 [56], GRI 3.0 [57], and NUIG 1.1 [58] models. All mechanisms are applicable over wide temperature ranges (300–5000 K) and are suitable for the pressure conditions used in previous experiments.

For the Aramco 3.0 [56] mechanism (160 species, 1104 reactions), the model is built upon a series of foundational studies and is well suited for representing C2–C3 alkene, diene, and alkyne oxidation chemistry. This combined mechanism is therefore appropriate for simulating alkene/diene/alkyne + N_2O combustion systems [63]. The DLR SynNG + NO [10] mechanism is designed for C0–C3/NO_X combustion systems and has been further optimized for C_2H_6/N_2O and C_2H_4/N_2O mixtures [10]. It incorporates the C0–C3 kinetic base of Methling et al. [64], which was optimized using extensive experimental datasets, including ignition delay times, species concentration profiles, and laminar burning velocities, resulting in a mechanism containing 165 species and 1410 reactions. For GRI 3.0 [57] (154 species, 1453 reactions), the CH-radical chemistry relevant to prompt-NO formation has been updated according to recent experimental measurements. The NUIG 1.1 [58] mechanism includes the C2–C7 alkene sub-mechanisms developed by Nagaraja et al. [65] and Dong et al. [66], along with propyne chemistry from Panigrahy et al. [67]. The combined NUIG 1.1 [58] model contains 2270 species and 11,613 reactions.

All four models contain comprehensive descriptions of N_2O chemistry and unsaturated hydrocarbon oxidation. Their validity has been demonstrated in previous experimental and kinetic studies on the ignition delay times of N_2O-containing and unsaturated hydrocarbon systems [8,11,19,20,23,68]. Additionally, all four mechanisms include reaction subsets relevant to common diluents such as N_2, He, Ar, and CO_2 and do not impose constraints on the fuel-equivalence ratio. The diluents and equivalence ratios used in this study have also been widely validated in prior experimental and modeling work [8,11,19,20,23,68], ensuring consistency with established kinetic behavior. These models are used herein to investigate the impact of the direct interacting reactions between N_2O and unsaturated hydrocarbons on the modeling results. Kinetic modeling is conducted using the LLNL-developed fast solver Zero-RK [69].

3. Results and discussion

3.1. Species and reaction sites

This study investigates the O-atom addition reactions of two alkenes (C_2H_4 and C_3H_6), one diene (C_3H_4-A) and two alkynes (C_2H_2 and C_3H_4-P) by nitrous oxide (N_2O), resulting in the formation of N_2 and their corresponding products. A total of six reaction pathways is explored, as summarized in Fig. 1. Specifically, C_2H_4 reacts with N_2O to form CH_3CHO and N_2 (Fig. 1(R1)). For C_3H_6, the oxygen atom of N_2O can be added at two distinct positions: the ν(S) site, yielding CH_3CH_2CHO (Fig. 1(R2)), and the ν(T) site, leading to the formation of CH_3COCH_3 (Fig. 1(R3)). For the diene, C_3H_4-A reacts with N_2O to generate CH_2CHCHO (Fig. 1(R4)). In the case of alkynes, C_2H_2 reacts with N_2O to produce CH_2CO (Fig. 1(R5)), while C_3H_4-P yields CH_3CHCO as the final product (Fig. 1(R6)).

The detailed reaction mechanisms and energy profiles for each system will be discussed in the following section.

3.2. Reaction path and potential energy surfaces

3.2.1. Alkenes

For alkenes, the reaction pathways leading to the corresponding products are generally similar. Taking R1 as an example, the reaction with N_2O proceeds via the formation of a reactant complex RC_1–1 prior to reaching the transition state TS_1–1, as can be seen in Fig. 2. In the transition state TS_1–1, the nitrogen and oxygen atoms of N_2O approach the two different carbon atoms of C_2H_4. Subsequently, both the N and O atoms form bonds with the different carbon atoms, resulting in a five-membered ring intermediate INT_1–1. Following this, the distance between N and O atoms is elongated, leading to the formation of TS_1–2. Thereafter, the N-C bond breaks, accompanied by a hydrogen atom transfer from the $-CH_2O$ moiety to the adjacent carbon atom, ultimately forming a $-CH_3$ group. This step, illustrated in Fig. 3, is particularly noteworthy because it features four concurrent bond rearrangements: cleavage of the N3–O5 and N4–C6 bonds, along with the breaking of the C1–H2 bond and the simultaneous formation of the H2–C6 bond. These coupled events ultimately lead to the formation of CH_3CHO and N_2. Along the reaction path, the nuclear repulsion energy exhibits distinct variations corresponding to each bond rearrangement. Upon rupture of the N3–O5 bond, the nuclear repulsion energy increases to –263.1781 Hartrees. Subsequent cleavage of the N4–C6 bond results in a decrease to –263.1786 Hartrees. As the H2 atom transfers from C1 to C6, the energy decreases further, reaching –263.3286 Hartrees at the end of the process.

For C_3H_6, the reaction follows an analogous pathway. However, the specific site of O-atom addition, namely either the ν(S) (R2) or ν(T) (R3) site on C_3H_6, determines the resulting products. Addition at the ν(S) site produces C_2H_5CHO, while addition at the ν(T) site leads to the formation of CH_3COCH_3, as illustrated in Figs. 4 and 5, respectively. The quantum chemistry calculations presented in Figs. 2, 4 and 5 support the reaction pathway proposed by Parmon et al. [32].

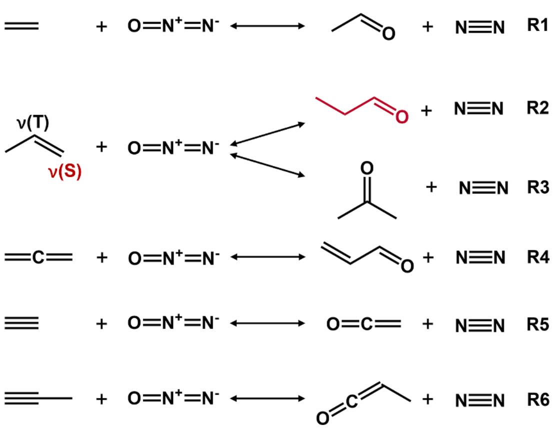

Fig. 1. The reaction sites and products for direct interaction of N_2O with (R1) C_2H_4 to form CH_3CHO, (R2) C_3H_6-ν(S) to form C_2H_5CHO, (R3) C_3H_6-ν(T) to form CH_3COCH_3, (R4) C_3H_4-A to form CH_2CHCHO (R5) C_2H_2 to form CH_2CO and (R6) C_3H_4-P to form CH_3CHCO.

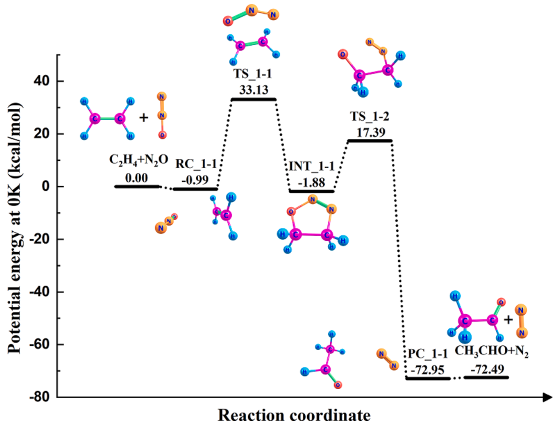

Fig. 2. The PES for O-atom addition reaction from N_2O to C_2H_4 forming CH_3CHO and N_2. All values are in *kcal/mol*.

3.2.2. Diene

The structural difference between diene and alkene is that the diene contains two C=C bonds, whereas the alkene contains only one. The reaction pathway for diene follows a similar mechanism to that of alkene, as shown in Fig. 6. For C_3H_4-A (R4), it is evident that the energy of the transition state TS_4–1 is higher than those of C_3H_6. Additionally, the energy barrier (E_{TS_X-2} – E_{INT_X-1}) for C_3H_4-A is higher than that of C_3H_6. This difference may be due to the presence of two C=C bonds, which increase the energy barrier.

3.2.3. Alkynes

For alkynes, the reaction pathways differ significantly from those of alkenes and diene. Taking C_2H_2 (R5) as an example, the N and O atoms of N_2O approach the two carbon atoms of C_2H_2 to form the transition state TS_5–1 via the reactant complex RC_5–1, as can be seen in Fig. 7. In this step, the C≡C triple bond is cleaved to form C=C double bond, and new N-C and O-C bonds are formed, yielding a five-membered ring intermediate INT_5–1. Subsequently, the N-O bond in INT_5–1 breaks via TS_5–2, generating another intermediate, INT_5–2. This step is notably different from the alkene and diene pathways, where both C-N and N-O bonds typically cleave in a single transition state. In contrast, for alkynes, only the N-O bond is cleaved at this stage. Following this, the C-N bond in INT_5–2 is elongated, leading to the formation of transition state TS_5–3. Eventually, the C1-N5 bond breaks, and H4 atom transfer occurs from the -CHO moiety to the adjacent -CH group, resulting in the final products: CH_2CO and N_2, via the product complex PC_5–1. The detailed reaction pathway from INT_5–2 to PC_5–1 is illustrated in Fig. 8. For the nuclear repulsion energy, the C1-N5 bond breaks with the energy increases to 261.9829 Hartrees, and then the H4 transfers from C3 to C1 with the energy decreases to -262.1056 Hartrees.

For C_3H_4-P (R6), although its C≡C triple bond provides two potential sites for O-atom addition, the reaction proceeds preferentially via the terminal carbon atom, ultimately yielding CH_3CHCO and N_2 as the final products, as shown in Fig. 9. The overall reaction pathway closely resembles that of C_2H_2 and therefore will not be described in detail here. Compared with the C_3H_4-A isomer (R4), the transition state TS_6–1 clearly lies lower in energy than TS_4–1, with a difference of 1.44 kcal/mol. In addition, the C_3H_4-P isomer exhibits one additional reaction pathway compared with C_3H_4-A.

Overall, the uncertainties of the stable species and transition states are taken as ±0.5 and ±1.0 kcal/mol, respectively, following the recommendations of Sivaramakrishnan et al. [70].

3.2.4. Validation of determined reaction pathways

To validate the obtained results, this study compares the PES and reaction profile for C_2H_2 (R5) with those reported by Karami et al. [34], who employed the B3LYP/6–311++G(3df,3pd) and CCSD(T) levels of

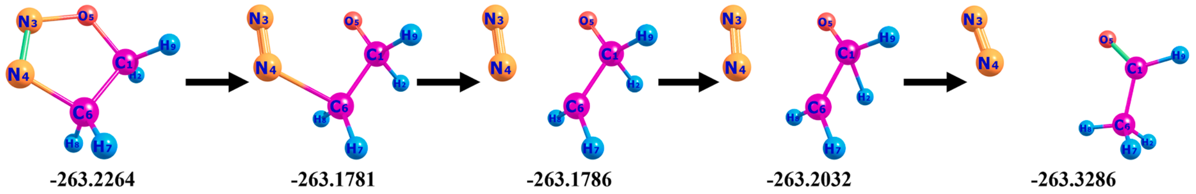

Fig. 3. The reaction path from INT_1–2 to PC_1–1 and the nuclear repulsion energy (Hartree) of 4 reaction steps in this reaction path from IRC.

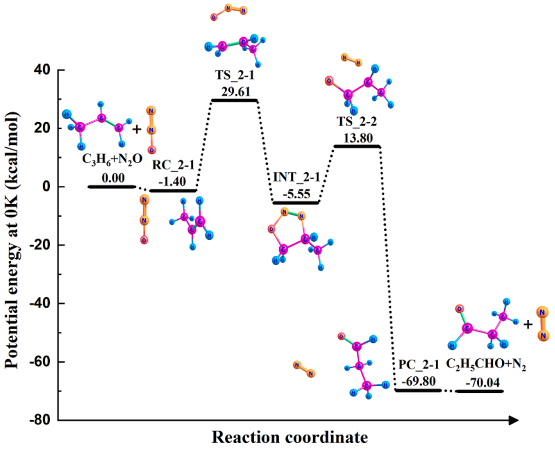

Fig. 4. The PES for O-atom addition reaction from N_2O to C_3H_6 on the ν(S) site (R2), forming C_2H_5CHO and N_2. All values are in *kcal/mol*.

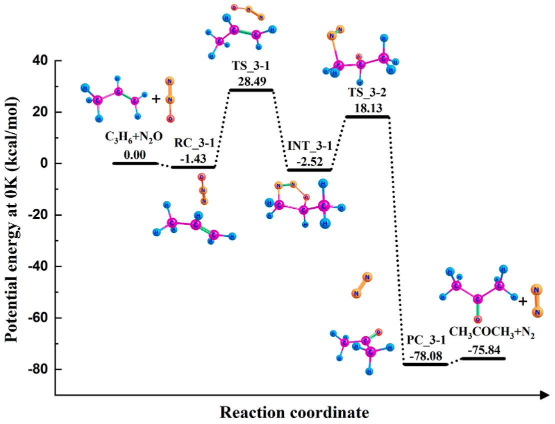

Fig. 5. The PES for O-atom addition reaction from N_2O to C_3H_6 on the ν(T) site (R3), forming CH_3COCH_3 and N_2. All values are in *kcal/mol*.

theory. These differ from the M06–2X/6–311++G(d,p) and CCSD (T)-CBS methods adopted in the present work. Compared with the conventional B3LYP functional, M06–2X incorporates a larger fraction of Hartree–Fock exchange (54 %) and includes a kinetic-energy-density term, enabling a more accurate description of nonlocal exchange and medium-range correlation effects [38]. Such features enhance the ability to capture reaction barriers, radical intermediates, and noncovalent interactions, all of which are crucial for the N_2O + alkene/diene/alkyne interaction reactions involving open-shell transition states. Consequently, M06–2X provides improved kinetic accuracy over B3LYP and is therefore more suitable for the present study. Regarding computational efficiency, the M06–2X method is only slightly slower than B3LYP. Although the 6–311++G(3df,3pd) basis set generally affords greater accuracy than 6–311++G(d,p) because of its extended polarization and diffuse functions (notably for radicals, excited states, or systems with strong polarization), the M06–2X/6–311++G(d,p) combination strikes an effective balance between computational cost and accuracy for the N_2O–alkene/diene/alkyne reactions examined herein. Despite the differences in theories, the overall reaction pathway obtained here is consistent with that reported by Karami et al. [34], as can be seen in Fig. 10. Notably, this study includes both the reactant complex (RC) and product complex (PC), which were not identified in [34].

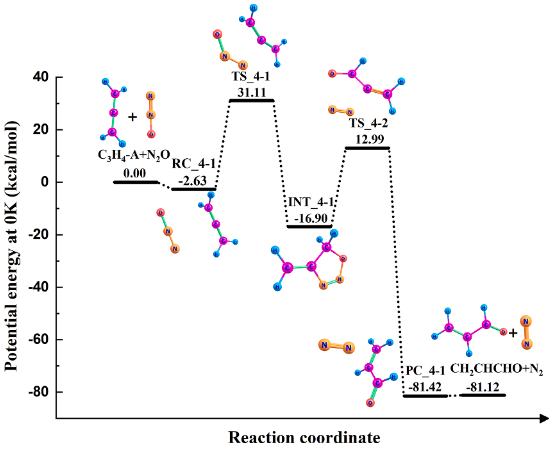

Fig. 6. The PES for O-atom addition reaction from N_2O to C_3H_4-A on the ν(S) site (R4), forming CH_3COCH_3 and N_2. All values are in *kcal/mol*.

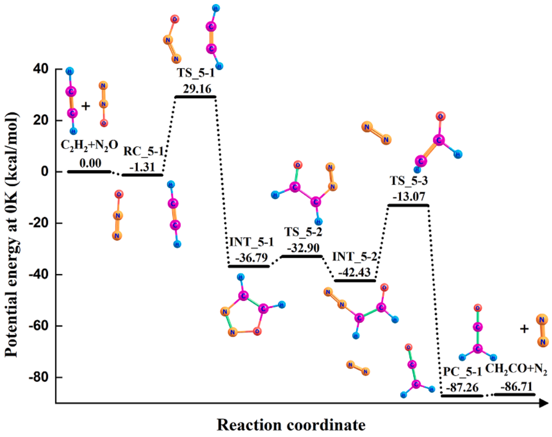

Fig. 7. The PES for O-atom addition reaction from N_2O to C_2H_2 forming CH_2CO and N_2 (R5). All values are in *kcal/mol*.

In terms of energy comparison, the calculated energies for TS_5–1, TS_5–3 and the product are in good agreement between the two studies, with discrepancies within 1 kcal/mol. However, a significant difference is observed in the region between INT_5–1 and INT_5–2. The potential energies calculated in this study are consistently higher than those reported by Karami et al. [34], with energy differences of 4.96, 3.70, and 3.74 kcal/mol for INT_5–1, TS_5–1, and INT_5–2, respectively.

To investigate the source of this discrepancy, the geometries of these three key structures are compared, with the results summarized in Fig. 11. For INT_5–1, the largest structural difference lies in the N-O

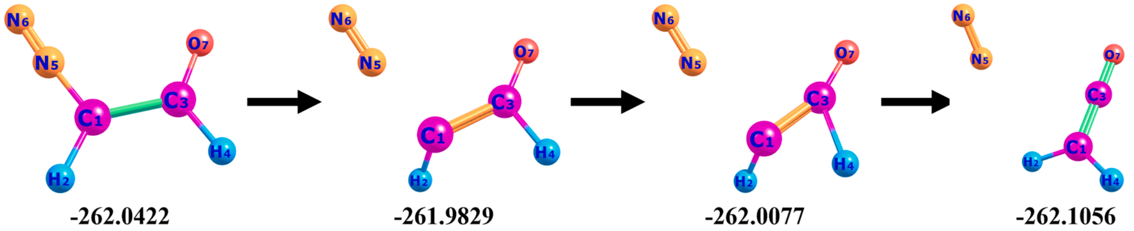

Fig. 8. The reaction path from INT_5–2 to PC_5–1 and the nuclear repulsion energy (Hartree) of 3 reaction steps in this reaction path from IRC.

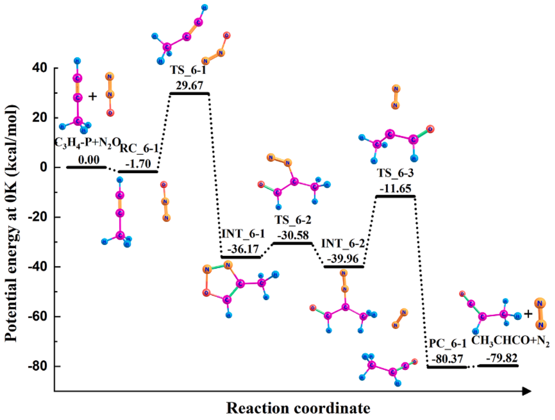

Fig. 9. The PES for O atom addition reaction from N_2O to C_3H_4-P forming CH_3CHCO and N_2 (R6). All values are in *kcal/mol*.

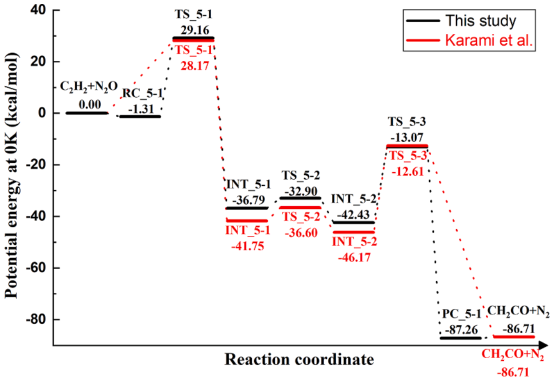

Fig. 10. Comparison of PES for the O-atom addition reaction from N_2O to C_2H_2, forming CH_2CO and N_2 (R5), between this study (black line) and the results reported by Karami et al. [34] (red line). All energy values are given in *kcal/mol.*

bond length, which is 1.395 Å in this study and 1.453 Å in [34]. For TS_5–2, the N-O bond lengths are 1.910 Å in this study and 1.862 Å in [34], and a significant difference is also found in the ∠NNC bond angle, with 124.3° in this study and 98.1° in [34]. In contrast, the geometries of INT_5–2 in both studies are very similar, with differences in bond lengths and angles within 0.01 Å and 2°, respectively. This study also compares the vibrational frequencies and T1 diagnostic values of the three structures with those reported by Karami et al. [34] in Table 2. The results show only minor differences. Then, in this work, the geometries of INT_5–1, TS_5–2, and INT_5–2 are re-optimized using the M06–2X method based on the initial structures reported by Karami et al. [34]. However, only the intermediate structures INT_5–1 and INT_5–2 can be successfully optimized, whereas TS_5–2 cannot be optimized. Subsequently, single-point energies of INT_5–1 and INT_5–2 are calculated at the CCSD(T)/CBS level. The resulting potential energies of INT_5–1 and INT_5–2 show excellent agreement with the energy profile obtained in this study. Notably, the T1 diagnostic values from this study are lower than those reported by Karami et al. [34], suggesting a more reliable single-reference description.

The discrepancies in geometries, frequencies, and potential energies between the two studies can largely be attributed to differences in the optimization methods: M06–2X/6–311++G(d,p) in this study versus B3LYP/6–311++G(3df,3pd) in [34]. For the single point energy calculation, the specific level of CCSD(T) used by Karami et al. [34] was not reported, which might also contribute to the observed differences. These methodological differences likely account for the deviations seen in the reaction pathway from INT_5–1 to INT_5–2.

3.2.5. *The reason for the different reaction steps between alkenes & diene and alkynes*

As mentioned above, when alkenes and diene react with N_2O, they first form five-membered ring intermediates (INT_X-1, X=1, 2, 3, etc.). Subsequently, both the N3-O1 bond and the N2-C5 bond break, followed by an H atom shift, ultimately leading to product formation. In contrast, for alkynes, the reaction also begins with the formation of five-membered ring intermediates (INT_X-1), but only the N3-O1 bond breaks at this stage, yielding new intermediates (INT_X-2). Through a distinct sub-reaction, these intermediates eventually convert into the final products. To explore the different reaction steps between alkenes & diene and alkynes, this study further analyzes the geometries of the intermediate structures: INT_X-1 of (a) alkenes, (b) diene and (c) alkynes.

It is evident in Fig. 12 that for all intermediate structures, the lengths of the N3-O1 bonds are very similar, with differences within 0.012 Å, indicating that the energy required to cleave the N3-O1 bond is nearly the same across systems. However, a significant difference lies in the N2-C5 bond length: in alkene intermediates, the N2-C5 bond is approximately 1.480 Å, whereas in alkyne intermediates, it is about 1.381 Å, with a difference of around 0.1 Å. The N2–C5 bond length in diene intermediates lies between these two values. Since bond length is inversely related to bond dissociation energy, a shorter N2-C5 bond generally corresponds to a stronger bond due to greater orbital overlap and increased bond stability. This suggests that breaking the N2-C5 bond in alkyne intermediates requires more energy than in alkene and diene intermediates. Consequently, the five-membered ring intermediates of alkenes and diene can break both the N2-C5 and N3-O1 bonds in a single transition state, while those of alkynes can only cleave the N3-O1 bond at that stage.

3.3. *Rate coefficients*

3.3.1. *Uncertainty analysis*

Based on the calculated potential energy surfaces for all reactions, the corresponding rate coefficients are determined and subsequently fitted to Arrhenius expressions. The uncertainty analysis follows the approaches from Xing et al. [71] and Sivaramakrishnan et al. [70], who demonstrated that TS energies and the collisional energy-transfer parameter (ΔE_{down}) are the dominant sources of uncertainty in overall rate coefficients. To quantify these effects, the present study perturbs the energies of TS_X-1, TS_X-2, TS_X-3 (X can be 1, 2, 3, etc.; e.g., TS_1–1) for the unsaturated hydrocarbon + N_2O reactions by ±1 kcal/mol and

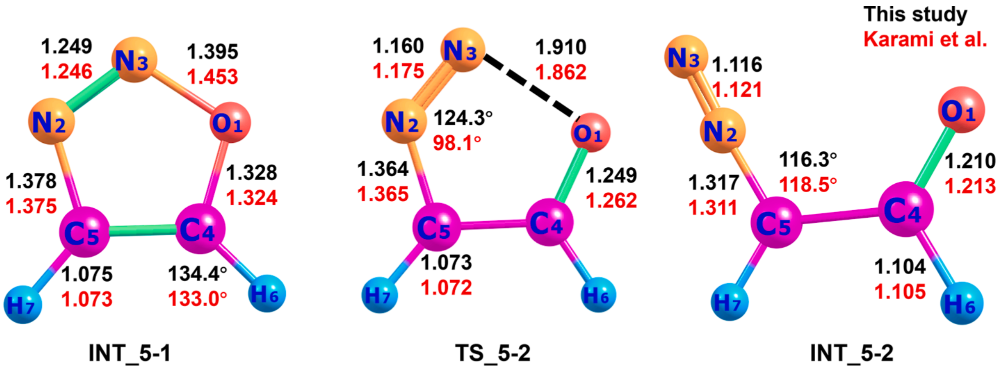

Fig. 11. Geometries of the intermediate structures INT_5–1 and INT_5–2, and the transition state TS_5–2, as obtained in this study (black text) and by Karami et al. [34] (red text).

Table 2
Comparison of the frequencies and T1 diagnostic for INT_5–1, TS_5–2, and INT_5–2, between this study and Karami et al. [34]. All energy values are given in *kcal/mol.*

	Frequencies of this study and Karami et al. [34] (cm^{-1})	T1 diagnostic (this study)	T1 diagnostic (Karami et al. [34])
INT_5–1	629[591], 711[674], 762[677], 821[775], 888[801], 963[940], 1006[969], 1113[1117], 1159 [1145], 1177[1183], 1394 [1316], 1491[1392], 1599 [1534], 3313[3317], 3336 [3338]	0.017	0.018
TS_5–2	-354[-370], 522[473], 598 [529], 700[656], 751[705], 875 [851], 951[890], 1074[1066], 1133[1095], 1257[1267], 1374 [1356], 1555[1467], 1901 [2103], 3170[3180], 3350 [3358]	0.028	0.029
INT_5–2	155[152], 272[247], 444[377], 512[437], 605[535], 816[810], 987[978], 1016[989], 1175 [1148], 1378[1391], 1423 [1423], 1786[1700], 2308 [2360], 3001[3002], 3290 [3294]	0.018	0.020

varies ΔE_{down} as 200±100 (±50 %) cm^{-1}. The rate coefficients are then recalculated under each perturbed condition. An uncertainty factor, f, is further determined as

$$f = \sqrt{\frac{k_{max}}{k_{min}}}$$

where k_{max} and k_{min} are the recomputed rate coefficients corresponding to the upper and lower bounds of the perturbed TS energies and ΔE_{down}, respectively [72].

The effects of individual uncertainty sources (e.g. TS_X-1±1 kcal/mol, TS_X-2±1 kcal/mol, TS_X-3±1 kcal/mol, or ΔE_{down} = 200±100 (±50 %) cm^{-1} are shown in Figs. S1–S6. In general, all sources of uncertainty exert significant influence at low temperatures, with their impacts diminishing as temperature increases (Figs. S1–S6). Among these factors, perturbation of TS_X-1 produces the strongest effect (Figs. S1(b)–S6(b)), yielding uncertainty factors between 3.90 and 5.50 at low temperatures. For alkenes and diene (Figs. S1–S4), ΔE_{down} and TS_X-2 exert secondary influences, associated with uncertainty factors ranging from 1.30 to 2.25 at low temperatures. For alkynes (Figs. S5 and S6), an interesting trend emerges: only TS_X-1 meaningfully affects the rate coefficients, while all other parameters exhibit negligible influences.

Based on the single-parameter analysis, the overall uncertainty in the rate coefficients is assessed by simultaneously increasing all TS energies by +1 kcal/mol with ΔE_{down} = 300 cm^{-1}, as well as by simultaneously decreasing all TS energies by −1 kcal/mol with ΔE_{down} = 100 cm^{-1}. The resulting uncertainty ranges are illustrated in Fig. 13. All reactions exhibit substantial uncertainty at low temperatures, whereas the rate coefficients converge at high temperatures (e.g., 2000 K), becoming nearly identical across all perturbation conditions. The overall uncertainty in the rate coefficients is approximately ±1 order of magnitude ($cm^3mol^{-1}s^{-1}$). For alkenes and dienes, the uncertainty remains high at low temperatures, with the largest uncertainty factor of ~17 observed for C_3H_6-ν(T) (R3), while C_2H_4 (R1) shows the smallest factor of ~9. For alkynes, the uncertainty factors for C_2H_2 (R5) and C_3H_4-P (R6) are comparable, both around 5.4.

3.3.2. *Rate coefficients analysis*

The rate coefficients obtained in this study are presented in Fig. 14 and summarized in Table 3. For alkenes, at low temperatures (e.g. 298 K), the rate coefficient of C_2H_4 (R1) is lower than those of C_3H_6 (R2, R3), with the values for different reactive sites of C_3H_6 being comparable. Among these, the ν(S) site of C_3H_6 (R2) exhibits the highest rate coefficient. However, as the temperature increases, the rate coefficients of C_2H_4 (R1) and the ν(T) site of C_3H_6 (R3) surpass that of the ν(S) site from C_3H_6 (R2), which can be attributed to the influence of 1-D hindered rotor effects at elevated temperatures. For the diene, the rate coefficient of C_3H_4-A (R4) is comparable to that of C_2H_4 (R1), but it is more than an order of magnitude lower than those of C_3H_6 (R2, R3). For alkynes, the rate coefficient of C_2H_2 (R5) remains higher than that of C_3H_4-P (R6) across the entire temperature range. Moreover, alkynes generally exhibit higher rate coefficients than alkenes and dienes, particularly at low temperatures. At 298 K, the rate coefficients for alkynes and alkenes & dienes are approximately 10^{-10} $cm^3mol^{-1}s^{-1}$ and 10^{-12} $cm^3mol^{-1}s^{-1}$, respectively, with a difference of about two orders of magnitude. As temperature increases, this gap narrows to within one order of magnitude at 2000 K. Moreover, the rate coefficient of C_3H_4-P (R6) is significantly higher than that of C_3H_4-A (R4), indicating that the reaction pathway of C_3H_4-P (R6) is more favorable.

3.4. *Model implementation and implications*

3.4.1. *Ignition delay time and uncertainty analysis*

To evaluate the impact of newly introduced reaction pathways on model performance, autoignition simulations are conducted under conditions of 40 bar pressure, fuel-equivalence ratio of 1, and a temperature range of 800–1450 K. The ignition timing is defined as the time corresponding to the maximum pressure rise rate:

$$Ignition\ Timing = t(dp/dt)_{max}.$$

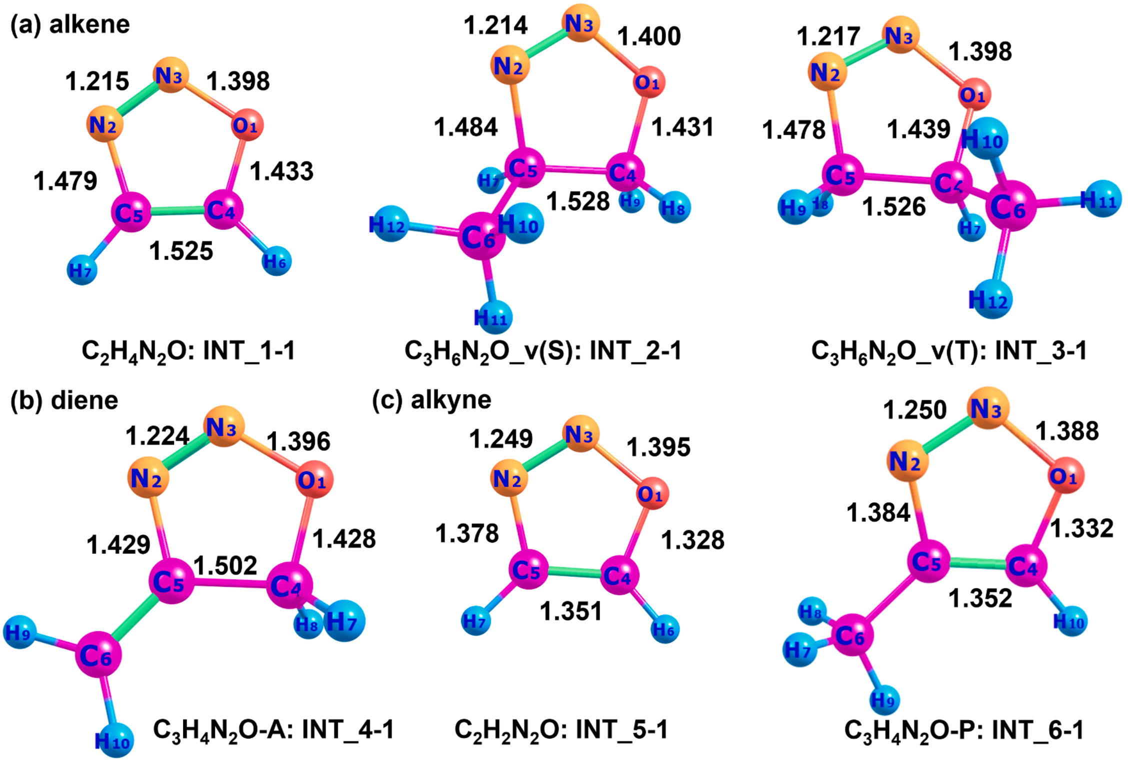

Fig. 12. Geometries of the intermediate structures (a) alkenes: INT_1–1, INT_2–1, INT_3–1, (b) diene: INT_4–1 and (c) alkynes: INT_5–1, INT_6–1.

The IDT is defined as the time interval between the initial state (temperature T_0 and pressure p_0) and ignition timing. Simulation results obtained with the original mechanisms are labeled as "Original", while those obtained with the updated mechanisms incorporating the new reaction pathways are labeled as "Updated". Based on the uncertainty analysis of rate coefficient presented in Section 3.3.1, the uncertainty range of the updated IDTs is determined by propagating the uncertainty of the rate coefficients into the kinetic models. The relative change between the original and updated IDTs is then quantified. A comparative analysis of these results is provided below.

As shown in Figs. 15, 16, and S7–S9, the uncertainty ranges of all reaction-specific IDTs remain within a factor of three. It is also evident that the IDTs predicted by the original mechanisms fall outside the uncertainty bounds of the updated mechanisms, which demonstrates that the updated IDTs are valid and significantly alter the reactivity of N_2O–unsaturated hydrocarbon chemistry, particularly at low temperatures. This indicates that the IDT uncertainty arising from the rate coefficient uncertainty of the new N_2O and unsaturated hydrocarbon reactions is much smaller than the impact introduced by the new reaction pathways themselves.

A comparison of the original and updated IDTs (Figs. 15, 16, and Figs. S7–S9) shows that the addition of O atoms from N_2O noticeably affects the ignition behavior of C_2H_4, C_3H_6, C_3H_4-A, C_2H_2, and C_3H_4-P, particularly in the low-temperature regime. At high temperatures, the IDTs predicted by both the original and updated mechanisms converge, and the differences among the four models become negligible. In contrast, at low temperatures, the updated mechanisms consistently predict shorter IDTs than their original counterparts, demonstrating that the newly introduced pathways enhance low-temperature autoignition reactivity.

For example, the relative change in C_2H_4 IDT between the original and updated mechanisms exceeds 40 % for Aramco 3.0 [56], GRI 3.0 [57], and NUIG 1.1 [58] models at low temperatures (Fig. 15(a), 15(c), and 15(d)), and the magnitude of this change decreases as temperature increases. For the DLR SynNG + NO [10] mechanism, the relative change is also around 15 % (Fig. 15(b)) at low temperatures. For C_2H_2, the relative IDT changes exceed 70 % in the low-temperature region. These examples highlight the substantial impact of the newly introduced reaction pathways.

Notably, for species such as C_3H_6, C_3H_4-A, C_2H_2, and C_3H_4-P, the updated models are able to predict IDTs at lower temperatures, which is not achievable with the original models. For instance, in the case of C_2H_2, as shown in Fig. 16 (c), the original GRI 3.0 [57] model can only predict IDTs at temperatures above 1000 K, which is insufficient for capturing the low-temperature chemistry of the fuel system. However, the incorporation of the new reaction pathways addresses this limitation, enabling the updated GRI 3.0 [57] model to predict IDTs as low as 800 K (the 800 K point is not shown in the figure). This observation suggests that the newly introduced reaction pathways are not only influential but also likely to dominate the low-temperature ignition chemistry. Furthermore, except for C_3H_4-A, the IDTs predicted by the updated models exhibit better agreement with each other than those predicted by the original models, demonstrating improved consistency across different mechanisms.

3.4.2. Comparison of ignition delay time and laminar burning velocity between model prediction and experimental results

To verify the impact of the newly introduced reaction pathways, the IDTs predicted by both the original and updated models are further compared with existing experimental data. The onset of ignition is defined using the same criteria of the corresponding experimental studied referenced. For the intermediate- and high-temperature ranges, the simulation results are compared with experimental measurements from Naumann et al. [8], conducted using a shock tube, as shown in Figs. 17, S10 and S11. The experimental conditions are set at 1, 4, and 16 bar, fuel-equivalence ratio of 1, and mixture composition of 20 % C_2H_4 and N_2O diluted in 80 % N_2. The simulated ignition timing is consistent with the experimental criterion as: $Ignition\ Timing_{simulation} = t([CH^*]_{max})$. As can be seen in Fig. 17, the IDTs predicted by all four original models show good agreement with the experimental data in the temperature

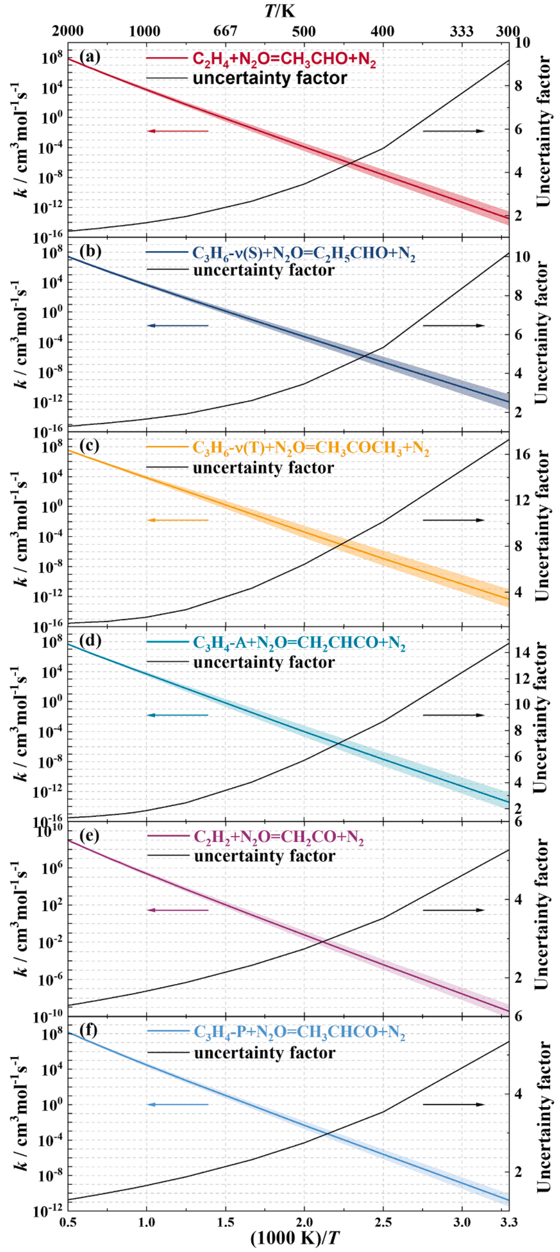

Fig. 13. Span of the calculated rate coefficients and associated uncertainty factors for the reactions of (a) C_2H_4+N_2O (R1), (b) C_3H_6-ν(S)+N_2O (R2), (c) C_3H_6-ν(T)+N_2O (R3), (d) C_3H_4-A+N_2O (R4), (e) C_2H_2+N_2O (R5), and (f) C_3H_4-P+N_2O (R6), evaluated under two perturbed conditions: (1) +1 kcal/mol applied to all transition-state energies with $\Delta E_{down} = 300$ cm^{-1}, and (2) −1 kcal/mol applied to all transition-state energies with $\Delta E_{down} = 100$ cm^{-1}. Light-shaded region represents the uncertainty of the rate coefficients.

range of 1250–1650 K. However, when temperature is below 1250 K, notable discrepancies emerge between original model predictions and experimental observations. The largest deviation is observed in the original GRI 3.0 [57] model, which overpredicts the IDT by approximately one order of magnitude. In contrast, the original DLR SynNG + NO [10] model yields predictions that are more consistent with the experimental data. For the updated models, the predicted IDTs are uniformly lower than those of their original counterparts at medium temperatures, indicating enhanced alignment with the experimental results. At lower pressures (1 and 4 bar), as shown in Figs. S10 and S11, the updated and original models yield nearly identical IDTs at high temperatures, and both reproduce the experimental trends reasonably well. Nevertheless, at 1 bar, the experimentally measured IDTs are shorter than the simulated values in the high-temperature regime.

This study further compares the simulation results with the experimental IDTs reported by Yang et al. [21] obtained using a rapid compression machine (RCM) under high-pressure and high-temperature conditions. The experiments were conducted at compressed temperatures $T_C = 1192-1266$ K and a compressed pressure $p_C = 45$ bar, with equivalence ratios of 1.0 and 0.5 and a C_2H_4 mole fraction of 0.25 %. The simulation conditions are set identical to the experimental setup, and the simulated ignition timing is defined as $Ignition\ Timing_{simulation} = t(dp/dt)_{max}$. The comparison results are shown in Fig. S12. It can be observed that the IDTs predicted by the updated models are very close to those of the original models, and the simulated IDTs are in reasonable agreement with the experimental measurements. However, both the original and updated models fail to reproduce the experimental trend accurately. This indicates that the reactions calculated in this work have a limited influence on ignition behavior under high-temperature conditions, regardless of pressure. Moreover, the inability of existing mechanisms to accurately capture the IDT trends of the C_2H_4/N_2O system may be attributed to the inherent complexity of C_2H_4/N_2O chemistry.

For low-temperature conditions, only one experimental study is available. In this work, the IDTs are compared with the experimental measurements reported by Zhang et al. [11] that were obtained in an RCM under the conditions of $T_C = 885-940$ K, $p_C = 3$ MPa, $\varphi = 1.05$ and 1.35 for N_2O-C_2H_4 propellants. The ignition timing used in all four kinetic models is defined as $Ignition\ Timing_{simulation} = t(dp/dt)_{max}$. As can be seen from Fig. 18, all original models significantly overpredict the IDTs compared to the experimental data, with discrepancies exceeding one order of magnitude. The limitation in predicting IDTs at low temperatures is observed for all four original models. This is particularly evident with the original Aramco 3.0 [56] model, which is only capable of predicting IDTs above 950 K and fails to cover the temperature range of the experimental data. By contrast, the updated models extend the predictive capability to lower temperatures and yield consistently shorter IDTs than the original models, resulting in much better agreement with the measurements. Moreover, the IDTs predicted by the updated models are more consistent with one another. This improvement is primarily attributed to the newly introduced reaction pathway, $C_2H_4 + N_2O = CH_3CHO + N_2$, which becomes a dominant pathway in the combustion chemistry of this fuel system at low temperatures.

However, noticeable discrepancies remain between the predictions of the updated mechanisms and the experimental data, which may be attributed to deficiencies in the low-temperature chemistry of the C_2H_4/N_2O system at mechanisms as well as uncertainties associated with heterogeneous effects. Regarding the former, the initiation reactions of the C_2H_4/N_2O system at low temperature are extremely hard to study due to the sequence of chemical reactions involved in the low-temperature oxidation of organic compounds [73]. Moreover, first-generation products are highly reactive and readily undergo rapid isomerization, decomposition, or secondary reactions with radicals before being sampled or detected. In addition, some oxidation intermediates are difficult to analyze using gas chromatography (GC), as they may decompose during separation within the GC column. The limited availability of experimental datasets under low-temperature conditions further constrains the validation and refinement of detailed kinetic models.

As a consequence, none of the four original mechanisms include reaction pathways describing interactions between N_2O and C_2H_4, and the present study only addresses part of this gap. Additional interaction pathways are therefore likely to exist but have not yet been identified. For example, the newly identified first-generation product CH_3CHO can further react with N_2O to form either CH_3COOH and N_2 or CH_2OHCHO and N_2, with the former channel exhibiting a lower reaction energy of 24.54 kJ/mol [74]. In addition, due to the presence of the C=C bond, another important first-generation intermediate in the C_2H_4/N_2O

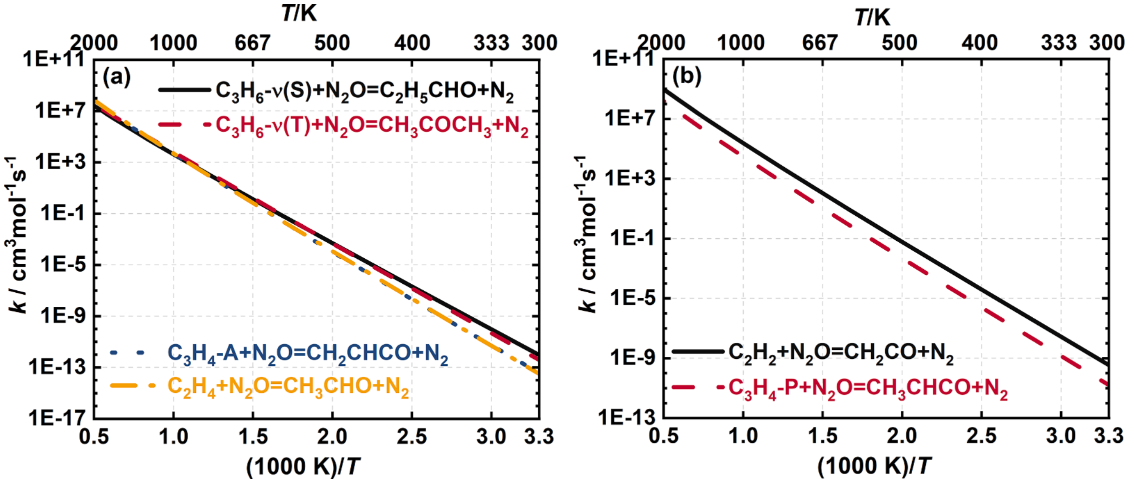

Fig. 14. The computed rate coefficients of O-atom addition from N_2O to (a) alkenes & diene and (b) alkynes, over the temperature range of 300–2000 K.

Table 3
Fitted parameters of A, n, and E, for the rate coefficients of O-atom addition from N_2O to alkenes, diene and alkynes, $k = AT^n \exp(-E_a/RT)$.

	Reaction species	Reaction	O-atom addition site	A (cm^3/mol*s)	n	E (cal/mol)
R1	Ethene and N_2O	C_2H_4+N_2O=CH_3CHO+N_2	–	1.033E+04	2.217	31,904.50
R2	Propene and N_2O	C_3H_6+N_2O=C_2H_5CHO+N_2	ν(S)	1.359E+04	1.955	29,130.57
R3	Propene and N_2O	C_3H_6+N_2O=CH_3COCH_3+N_2	ν(T)	1.150E+07	1.176	31,050.75
R4	Allene and N_2O	C_3H_4-A+N_2O=CH_2CHCO+N_2	–	2.259E+05	1.771	32,171.64
R5	Acetylene and N_2O	C_2H_2+N_2O=CH_2CO+N_2	–	2.122E+05	2.014	27,422.86
R6	Propyne and N_2O	C_3H_4-P+N_2O=CH_3CHCO+N_2	–	2.808E+04	2.069	28,264.10

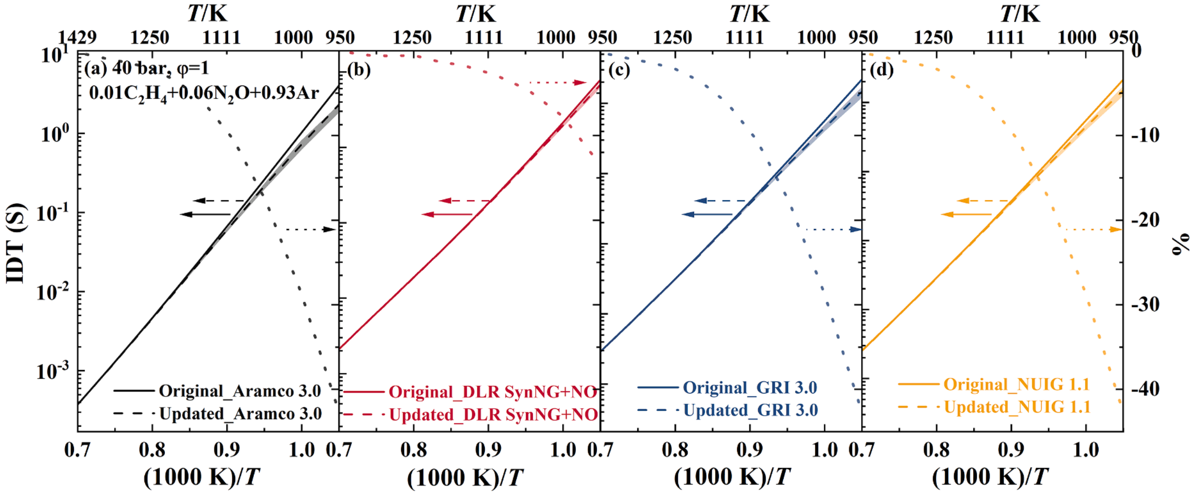

Fig. 15. The IDT of C_2H_4 mixed with N_2O and Ar predicted using the original (solid lines) and updated chemical kinetic mechanisms (dashed lines): (a) Aramco 3.0 [56], (b) DLR SynNG + NO [10], (c) GRI 3.0 [57], and (d) NUIG 1.1 [58]. The dashed curves are enclosed by the light-shaded region which represents the uncertainty of the updated IDTs, while the dotted line shows the relative change between the original and updated values. All simulations are performed at 40 bar, equivalence ratio of 1.0, and temperatures ranging from 950 to 1429 K.

system, C_2H_3 (discussed in Section 3.4.4), can also react with N_2O to form CH_2CHO and CH_3CO. These reactions may further contribute to the overall reactivity of the C_2H_4/N_2O system [1]. Supporting evidence for the complexity of N_2O–unsaturated hydrocarbon chemistry is provided by Karami et al. [34], who calculated several multi-step reaction pathways between C_2H_2 and N_2O leading to the formation of CHCOH, and HCN & HCNO. In particular, the formation of HCN &HCNO and CHCOH proceeds via five- and seven-step mechanisms, respectively, which are more complex than the pathways leading to CH_2CO. Although the first-step reaction is identical for these channels, differences arise in the subsequent steps, with the pathway leading to CH_2CO exhibiting the lowest energy barriers. Overall, these findings indicate that the chemistry of N_2O with unsaturated hydrocarbons and their products is extensive and urgently needs to be incorporated into detailed kinetic models. Therefore, further exploration of other interaction reaction pathways involving alkenes, dienes, alkynes and their reaction products with N_2O is essential for improving model accuracy. This will be investigated in our future study.

With respect to heterogeneous effects, Zhang et al. [11] reported that the temperature at the end of compression is the dominant factor

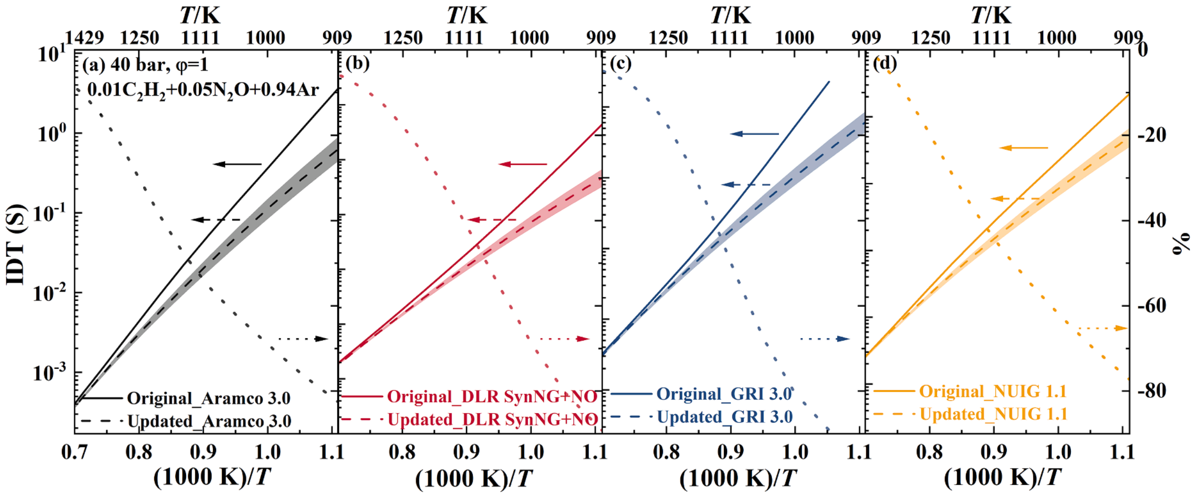

Fig. 16. The IDT of C_2H_2 mixed with N_2O and Ar predicted using the original (solid lines) and updated chemical kinetic mechanisms (dashed lines): (a) Aramco 3.0 [56], (b) DLR SynNG + NO [10], (c) GRI 3.0 [57], and (d) NUIG 1.1 [58]. The dashed curves are enclosed by the light-shaded region which represents the uncertainty of the updated IDTs while the dotted line shows the relative change between the original and updated values. All simulations are performed at 40 bar, equivalence ratio of 1.0, and temperatures ranging from 909 to 1429 K.

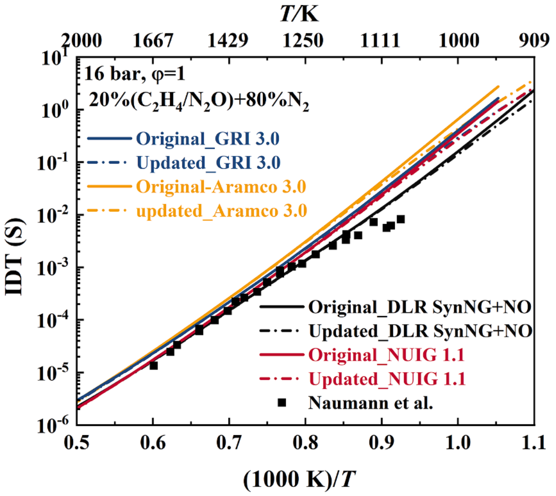

Fig. 17. The IDTs of C_2H_4 mixed with N_2O and N_2 using both the original and updated (a) Aramco 3.0 [56], (b) DLR SynNG + NO [10], (c) GRI 3.0 [57], and (d) NUIG 1.1 [58] models. The experiments were measured by Naumann et al. [8] using a shock tube. Simulations are conducted at pressure of 16 bar, equivalent ratio of 1.0, and temperatures of 900−2000 K. $Ignition\ Timing_{simulation} = t([CH^*]_{max})$.

affecting ignition delay time, with an overall uncertainty of approximately 10–15 %. Although Zhang et al. [11] did not explicitly report the measures used to minimize heterogeneous effects, their cited descriptions of the rapid compression machine setup [75–77] indicate that a crevice-design piston and an insulation jacket were employed to suppress roll-up vortices and to establish a more homogeneous temperature field. In addition, previous studies [75–77] using similar configurations incorporated a sufficient waiting period prior to compression to ensure complete fuel evaporation and mixing. Under these conditions, the fuel partial pressure remained well below its saturation vapor pressure, thereby guaranteeing complete vaporization and minimizing fuel loss due to wall adsorption negligible.

Furthermore, this study calculates the laminar burning velocities (LBVs) for comparison with the experimental results reported by Wang et al. [22] for C_2H_4/N_2O mixtures ($\phi = 0.2$–2.5) at initial pressure of 1 atm and initial temperature of 1 atm (Fig. S13). The results show no significant difference between the original and updated models, which is attributed to the fact that the reaction considered in this study has little effect at high temperatures.

3.4.3. Sensitivity analysis

To draw further insight into the impact of the O-atom addition into the unsaturated hydrocarbon from N_2O in the fuel systems, brute force sensitivity analysis is conducted on the main ignition delay time using constant volume simulations for the original & updated DLR SynNG + NO [10] and NUIG 1.1 [58] models, as both models predict IDTs that are in better agreement with the experimental results. The condition of this analysis is the same as the condition in Section 3.4.1, where the ignition timing is defined as the time corresponding to the maximum pressure rise rate:

$$Ignition\ Timing = t(dp/dt)_{max},$$

C_2H_4/N_2O and C_3H_6/N_2O are selected for analysis. The sensitivity analysis coefficient is defined as:

$$S_{rel} = \ln\left(\frac{\tau^{\Delta}}{\tau}\right) \Big/ \ln\left(\frac{k^{\Delta}}{k}\right) \tag{3}$$

where τ^{Δ} is the main IDT after multiplying the original rate constant by 2, i.e., $k^{\Delta} = 2 * k$, and τ is the original ignition delay time. It should be noted that the identity of the most sensitive reactions determined from sensitivity analyses remains unchanged when different perturbation factors are applied to the rate coefficients, as demonstrated in our previous studies [78,79]. A perturbation factor of 2 is adopted in this work because it provides the best numerical convergence for the IDT simulations. The negative sensitivity coefficient indicates the promotion effect, while the positive sensitivity coefficient indicates the inhibition effect. Therefore, Figs. 19 and 20 present the computed sensitivity coefficients of different fuels for the 16 most sensitive reactions.

Fig. 19 presents the sensitivity analysis results for C_2H_4. For both models, the most sensitive and strongly promoting reaction is the non fuel-specific reaction $N_2O(+M) = N_2 + O(+M)$. In the DLR SynNG + NO [10] model, Fig. 19(a), upon introducing the new pathway $C_2H_4 + N_2O = CH_3CHO + N_2$, this reaction emerges as the third most sensitive and promoting reaction. Notably, it also becomes the most sensitive fuel-specific reaction in the system. In addition, the subsequent reaction pathways involving CH_3CHO molecules (e.g., $CH_3CHO + CH_3 = CH_3CO + CH_4$) show increased sensitivity, which further contributes to the overall reactivity of the fuel system. The addition of O atom from N_2O to

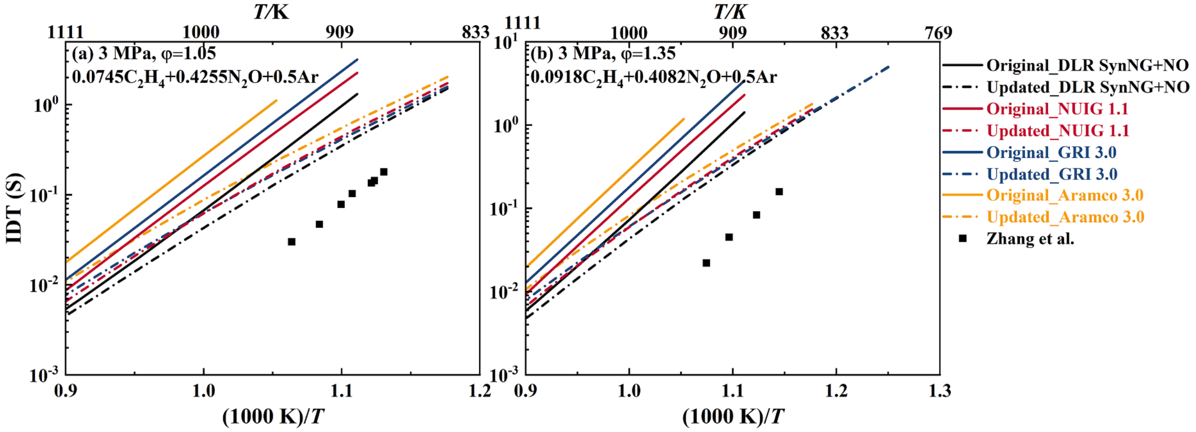

Fig. 18. The IDTs of C_2H_4 mixed with N_2O and Ar using both the original and updated (a) Aramco 3.0 [56], (b) DLR SynNG + NO [10], (c) GRI 3.0 [57], and (d) NUIG 1.1 [58] models. The experiments were measured by Zhang et al. [11] using a rapid compression machine (RCM). Simulations are conducted at pressure of 3 MPa, fuel-equivalence ratio of (a) 1.05 and (b) 1.35, and temperatures of 769–1100 K. *Ignition Timing*$_{simulation}$ $= t(dp/dt)_{max}$.

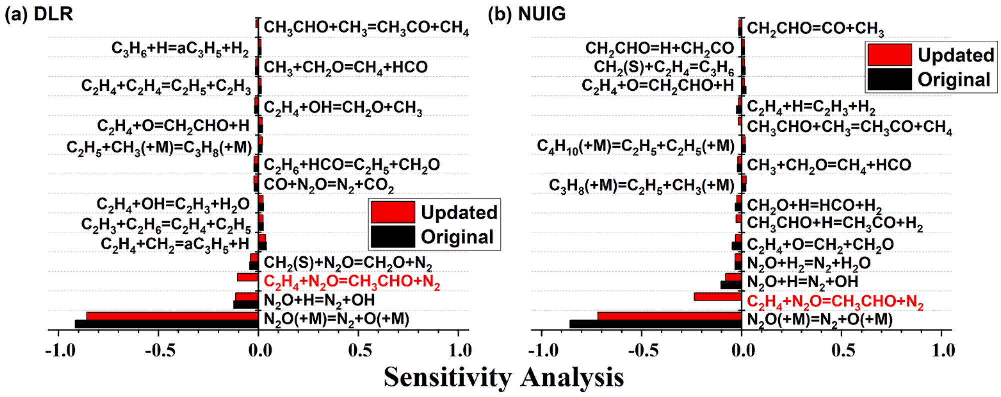

Fig. 19. The sensitivity analysis of simulated ignition delay time using the original mechanisms and the updated mechanisms with incorporating the calculations for reaction $C_2H_4 + N_2O$ (R1) at $p_C = 40$ bar, $T_C = 1000$ K, fuel-equivalence ratio of 1 by (a) DLR SynNG + NO [10] and (b) NUIG 1.1 [58] models, *Ignition Timing*$_{simulation}$ $= t(dp/dt)_{max}$.

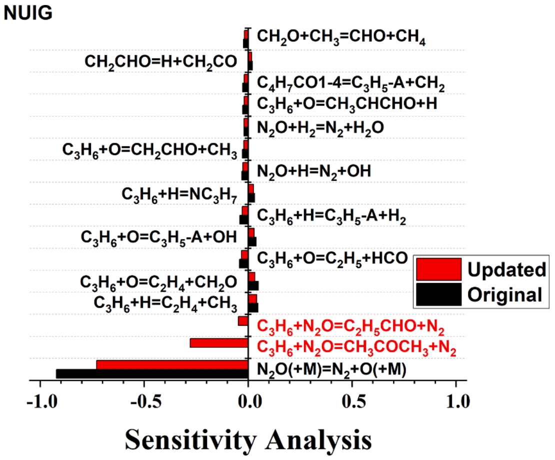

Fig. 20. The sensitivity analysis of simulated ignition delay time using the original mechanism and the updated mechanism with incorporating the calculations for reaction C_3H_6 +N_2O (R2 and R3) at $p_C = 40$ bar, $T_C = 1000$ K, fuel-equivalence ratio of 1 by NUIG 1.1 [58] model, *Ignition Timing*$_{simulation}$ $= t(dp/dt)_{max}$.

C_2H_4 consistently enhances reactivity by driving the reaction pathway toward CH_3CHO formation and branching. Additionally, the ratio of the most inhibiting fuel-specific reaction (i.e., $C_2H_4 + CH_2 = aC_3H_5 + H$) decreases in the updated model compared with the original model.

With the NUIG 1.1 [58] model, Fig. 19(b), a similar trend is observed. The new reaction pathway again emerges as the most sensitive fuel-specific reaction, and in this case, it ranks as the second most sensitive reaction overall. Additionally, the sensitivity coefficients of key follow-up reactions, such as $CH_3CHO + H = CH_3CO + H_2$ and $CH_3CHO + CH_3 = CH_3CO + CH_4$, increase significantly, further enhancing the reactivity of the fuel system. Overall, the pathway $C_2H_4 + N_2O = CH_3CHO + N_2$ and its subsequent reactions play a critical role in enhancing system reactivity to reduce IDTs, which are reflected in Figs. 15 and 18.

The sensitivity analysis results for C_3H_6 are shown in Fig. 20. As observed previously, the reaction $N_2O(+M) = N_2 + O(+M)$ remains the most sensitive and strongly promoting reaction. In the updated model, the newly introduced reaction pathways, $C_3H_6 + N_2O = C_2H_5CHO + N_2$ (R2) and $C_3H_6 + N_2O = CH_3COCH_3 + N_2$ (R3), emerge as the second and third most sensitive and promoting reactions, respectively. Notably, the inclusion of these pathways suppresses the influence of all dominant inhibiting reactions, such as $C_3H_6 + H = C_2H_4 + CH_3$, $C_3H_6 + O = C_2H_4 + CH_2O$, etc. By introducing additional low-temperature oxidation channels, these new reactions substantially enhance the overall reactivity of the fuel system.

3.4.4. Flux analysis

Flux analyses are performed using variable-volume simulations for C_2H_4 and C_3H_6 under the same conditions described in Section 3.4.3

(Figs. 19 and 20). The results, presented at 1 % fuel consumption, indicate the distribution of each reactant's consumption among the different identified pathways. Upon incorporating the new reaction pathway into the model, substantial changes in flux distributions are observed.

Fig. 21 shows the flux analysis results for C_2H_4 in the NUIG 1.1 [58] model at 1000 K. With the addition of the O-atom transfer pathway from N_2O to C_2H_4, the contributions from other C_2H_4 consumption pathways decrease, including certain reactions with reactivity-inhibiting effects, such as $C_2H_4 \rightarrow CH_2CHO$ and $C_2H_4 \rightarrow C_3H_6$, as shown in Fig. 14(b). In contrast, approximately 17.7 % of C_2H_4 is consumed via the newly added pathway $C_2H_4 + N_2O = CH_3CHO + N_2$. This pathway is identified as the most sensitive and strongly promoting fuel-specific reaction in the system. Its major subsequent reaction, $CH_3CHO \rightarrow CH_3CO$, also ranks among the most promoting reactions in the sensitivity analysis presented in Section 3.4.3, consuming approximately 82 % of CH_3CHO, the highest share among all CH_3CHO consumption routes. Consequently, the O-atom addition from N_2O to C_2H_4 and its subsequent oxidation sequence significantly shorten the ignition delay time. The results of C_2H_4 from DLR SynNG + NO [10] model (Fig. S14) exhibit a similar trend to the NUIG 1.1 [58] model, with quantitative differences observed: approximately 7.4 % of C_2H_4 is consumed through the new pathway in DLR SynNG + NO [10] model, leading to an increased CH_3CHO production rate and accelerated CH_3CO formation. These downstream processes directly contribute to the significant reduction in IDTs observed in Sections 3.4.1–3.4.2. In addition, the flux analysis results for C_3H_6 using the NUIG 1.1 [58] model show consistent results as C_2H_4, as shown in Fig. 22. The newly introduced reaction pathway, $C_3H_6 + N_2O = CH_3COCH_3 + N_2$ (R3), accounts for 20 % of the total C_3H_6 consumption and represents the most sensitive, strongly promoting fuel-specific reaction. Another sensitive and promoting pathway, $C_3H_6 + N_2O = C_2H_5CHO + N_2$ (R2), contributes an additional 2.4 % to the overall C_3H_6 consumption. Together, these reactions enhance the reactivity of the combustion system and lead to shorter IDTs. Based on these results, it is evident that CH_3CHO is a new first-generation product in the C_2H_4/N_2O combustion system, accounting for 17.7 % of the total flux in the updated model, Fig. 21. For the C_3H_6/N_2O combustion system, two additional first-generation products, C_2H_5CHO (2.4 %) and CH_3COCH_3 (20 %) are predicted in the updated model, Fig. 22. Based on this observation, we performed additional jet-stirred reactor (JSR) simulations using CHEMKIN, adopting the JSR configuration from Princeton University [80]. The simulation conditions are identical to those in Fig. 21, with the residence time (τ) set at 0.35 s. As shown in Fig. S15. The results indicate that the CH_3CHO mole fraction remains near zero below 750 K, then increases with temperature and reaches a maximum value of approximately 200 ppm at around 1000 K. This concentration level suggests that CH_3CHO should be readily detectable using experimental techniques such as GC. As the temperature further increases, the CH_3CHO mole fraction decreases and approaches zero at about 1200 K.

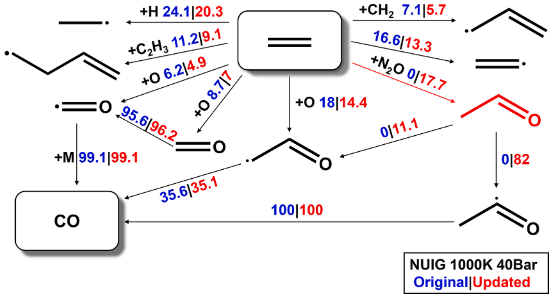

Fig. 21. The flux analysis using the original mechanism and the updated mechanism with incorporating the calculations for reaction $C_2H_4 + N_2O$ (R1) at $p_C = 40$ bar, $T_C = 1000$ K, fuel-equivalence ratio of 1 by NUIG 1.1 [58] model. Fluxes are computed at 1 % C_2H_4 consumption.

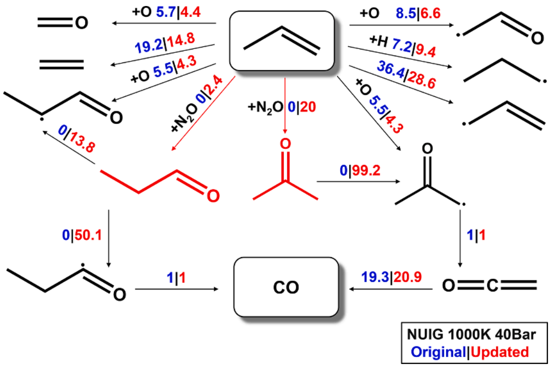

Fig. 22. The flux analysis using the original mechanism and the updated mechanism with incorporating the calculations for reaction $C_3H_6 + N_2O$ (R2 and R3) at $p_C = 40$ bar, $T_C = 1000$ K, fuel-equivalence ratio of 1 by NUIG 1.1 [58] model. Fluxes are computed at 1 % C_3H_6 consumption.

This behavior further confirms that the newly incorporated reaction R1 influences low-temperature chemistry, while its impact at high temperatures is minimal.

To further investigate the role of the reactions studied in this work under high-temperature conditions, flux analysis results for C_2H_4 and N_2O using the NUIG 1.1 model [58] at 1500 K are further conducted, with the results presented in Fig. S16. The flux distributions obtained with the updated model are very similar to those from the original model. It is evident that the dominant primary pathways at high temperature differ substantially from those under low-temperature conditions. Specifically, the channel leading to C_2H_3 formation dominates, accounting for approximately 60 % of the total flux, followed by the CH_2O and CH_2CHO formation pathways. This behavior contrasts with the low-temperature regime, where multiple major first-product channels coexist, including C_2H_5, CH_2CHO, CH_3CHO, and C_2H_3. Overall, the reaction investigated in this study plays a significant role in the low-temperature regime but has a negligible impact under high-temperature conditions.

4. Conclusions

This work characterizes new direct interaction pathways between N_2O and unsaturated hydrocarbons, covering C_2H_4, C_3H_6, C_2H_2, C_3H_4-A, and C_3H_4-P, through quantum chemistry calculations, comprehensive kinetic modeling, and experimental validations. These pathways have been missing from existing chemistry models and the corresponding rate coefficients have not been reported in the past. The key findings are as follows:

- The direct interaction pathways between N_2O and unsaturated hydrocarbons proceed via O-atom addition reactions from N_2O to unsaturated hydrocarbons in multiple steps, which first form a five-member ring intermediate and eventually lead to the production of N_2 and different products depending on the hydrocarbon type and the reaction site for O-atom addition. The major difference between alkenes & diene and alkynes lies in the decomposition pathway of the five-member ring intermediate, with the cleavage of N-C and N-O bonds and intramolecular H-atom transfer occurring in the same step for alkenes and diene, while in different consecutive steps for alkynes.
- The distinctly different interaction pathways between alkenes, dienes, and alkynes are further investigated via quantum mechanical analysis, which can be primarily attributed to the structural disparity of the five-membered ring intermediates with respect to the N-C bond length. Shorter and stronger N-C bonds are observed in alkyne intermediates than in alkene and diene intermediates (i.e., ~1.480 Å for alkenes and 1.429 Å for dienes vs. ~1.381 Å for alkynes

intermediates), resulting in the higher energy required for N-C bond cleavage for alkyne intermediates.

- The rate coefficients of the direct interacting reactions are further determined and incorporated into four different kinetic models. Autoignition modeling results highlight the significant promoting impact of the new reactions on model reactivity for all models, with the O-atom addition reactions from N_2O to unsaturated hydrocarbons emerging as the most sensitive fuel-specific promoting reaction. With the new reactions incorporated, the models' capability for autoignition simulation are extended to lower temperature ranges, with much better agreements obtained with experiments.
- The uncertainties of PES for stable species and transition states are assigned as ±0.5 and ±1.0 kcal/mol, respectively. For the rate coefficients, the perturbation of the first transition state energy has the most significant effect on the rate coefficients for all reactions, while ΔE_{down} and the second transition state energy have secondary influences, particularly for alkenes and dienes. Based on the uncertainty analysis of the IDTs, the IDTs predicted by the original mechanisms fall outside the uncertainty bounds of the updated mechanisms, demonstrating that the updated IDTs are valid and significantly improve the accuracy of the predictions.
- Flux analysis reveals that the addition of the new pathways reduces fuel consumption via the conventional inhibiting pathways, while enables new dominant pathways for fuel consumption that lead to the formation of aldehydes and ketones, with both promoting reactivity.

Novelty and significance statement

To date, direct kinetic interactions between unsaturated hydrocarbons and N_2O remain unknown and are missing from all existing chemistry models, despite the important roles of unsaturated hydrocarbons and N_2O as potential propellants for advanced propulsion systems (e.g. NOFBX) and key combustion intermediates in exhaust gas recirculation systems. This study is the first study that addresses these gaps by systematically quantifying the interaction kinetics between N_2O and three types of unsaturated hydrocarbons: alkenes, dienes, and alkynes, with rate parameters also determined via quantum chemistry computations. New and unique kinetic interactions are first revealed, with similarities and differences quantified across different reaction sites and unsaturated hydrocarbons, which can lead to the formation of either ketones or aldehydes, with both being important derivatives in combustion. Incorporating these new pathways and rate coefficients into four kinetic models consistently leads to a substantial reduction in predicted ignition delay times at low temperatures, bringing the simulations into closer agreement with experimental data. Uncertainty analyses of the potential energy surfaces, rate coefficients, and ignition delay times are performed to ensure the reliability of the results. These findings address the long-standing overprediction of low-temperature ignition delay times (IDTs) for unsaturated hydrocarbons/N_2O mixtures.

CRediT authorship contribution statement

Hongqing Wu: Writing – review & editing, Writing – original draft, Validation, Software, Formal analysis, Conceptualization. **Guojie Liang:** Writing – review & editing, Writing – original draft, Validation, Software, Formal analysis, Conceptualization. **Tianzhou Jiang:** Writing – review & editing, Validation, Formal analysis, Data curation. **Fan Li:** Writing – review & editing, Validation, Formal analysis, Data curation. **Yang Li:** Writing – review & editing, Validation, Formal analysis, Data curation. **Rongpei Jiang:** Writing – review & editing, Validation, Formal analysis, Data curation. **Ruoyue Tang:** Writing – review & editing, Validation, Formal analysis, Data curation. **Song Cheng:** Writing – review & editing, Writing – original draft, Supervision, Resources, Project administration, Conceptualization.

Declaration of competing interest

The authors declare that they have no known competing financial interests or personal relationships that could have appeared to influence the work reported in this paper.

Acknowledgments

The work described in this paper is supported by the Research Grants Council of the Hong Kong Special Administrative Region, China under 25210423 for ECS project funded in 2023/24 Exercise, the National Natural Science Foundation of China under 52406158, and the Natural Science Foundation of Guangdong Province under 2024A1515011486.

Supplementary materials

Supplementary material associated with this article can be found, in the online version, at doi:10.1016/j.combustflame.2026.114817.

References

[1] R. Tang, S. Cheng, Combustion chemistry of unsaturated hydrocarbons mixed with NOx: A review with a focus on their interactions, Energies 16 (2023) 4967.
[2] V. Zakirov, M. Sweeting, T. Lawrence, J. Sellers, Nitrous oxide as a rocket propellant, Acta Astronaut. 48 (2001) 353–362.
[3] D. Razus, Nitrous oxide: oxidizer and promoter of hydrogen and hydrocarbon combustion, Ind. Eng. Chem. Res. 61 (2022) 11329–11346.
[4] W. Pu, D. Sun, W. Fan, W. Pan, Q. Chai, X. Wang, Y. Lv, Cu-catalyzed atom transfer radical addition reactions of alkenes with α-bromoacetonitrile, Chem. Commun. 55 (2019) 4821–4824.
[5] E. Zamir, Y. Haas, R. Levine, Laser enhanced addition reactions between hydrogen halides and unsaturated hydrocarbons: an information–theoretic approach, J. Chem. Phys. 73 (1980) 2680–2687.
[6] T.J. Preston, G.T. Dunning, A.J. Orr-Ewing, S.A. Vazquez, Direct and indirect hydrogen abstraction in Cl+ alkene reactions, J. Phys. Chem. A 118 (2014) 5595–5607.
[7] C. Zhou, A. Farooq, L. Yang, A.M. Mebel, Combustion chemistry of alkenes and alkadienes, Prog. Energ. Combust. 90 (2022) 100983.
[8] C. Naumann, T. Kick, T. Methling, M. Braun-Unkhoff, U. Riedel, Ethene/nitrous oxide mixtures as green propellant to substitute hydrazine: reaction mechanism validation, Int. J. Energetic Mater. Chem. Propul. 19 (2020).
[9] L. Werling, F. Lauck, D. Freudenmann, N. Röcke, H. Ciezki, S. Schlechtriem, Experimental investigation of the flame propagation and flashback behavior of a green propellant consisting of N2O and C2H4, J. Energy Power Eng. 11 (2017) 735–752.
[10] C. Janzer, S. Richter, C. Naumann, T. Methling, Green propellants" as a hydrazine substitute: experimental investigations of ethane/ethene-nitrous oxide mixtures and validation of detailed reaction mechanism, CEAS Sp. J. 14 (2022) 151–159.
[11] F. Zhang, H. Chen, J. Feng, D. Zheng, Experimental investigation of auto-ignition of ethylene-nitrous oxide propellants in rapid compression machine, Fuel 288 (2021) 119688.
[12] R. Taylor, Safety and performance advantages of nitrous oxide fuel blends (NOFBX) propellants for manned and unmanned spaceflight applications, Safer Sp. Safer World 699 (2012) 67.
[13] X. Yang, X. Hong, W. Dong, Investigation on self-pressurization and ignition performance of nitrous oxide fuel blend ethylene thruster, Aerosp. Sci. Technol. 82 (2018) 161–171.
[14] S. Cheng, C. Saggese, S.S. Goldsborough, S.W. Wagnon, W.J. Pitz, Unraveling the role of EGR olefins at advanced combustion conditions in the presence of nitric oxide: ethylene, propene and isobutene, Combust. Flame 245 (2022) 112344.
[15] Q. Peng, D. Huo, C.M. Hall, A comparison of neural network-based strategies for diesel engine air handling control, in: 2022 American Control Conference (ACC), IEEE, 2022, pp. 3031–3037.
[16] Q. Peng, D. Huo, C.M. Hall, Neural network-based air handling control for modern diesel engines, Proc. Inst. Mech. Eng., Part D 237 (2023) 1113–1130.
[17] S. Cheng, C. Saggese, S.S. Goldsborough, S.W. Wagnon, W.J. Pitz, Chemical kinetic interactions of NO with a multi-component gasoline surrogate: experiments and modeling, Proc. Combust. Inst. 39 (2023) 531–540.
[18] A. Trenwith, The kinetics of the oxidation of ethylene by nitrous oxide, J. Am. Chem. Soc. (1960) 3722–3726.
[19] F. Deng, Y. Pan, W. Sun, F. Yang, Y. Zhang, Z. Huang, Comparative study of the effects of nitrous oxide and oxygen on ethylene ignition, Energy Fuels 31 (2017) 14116–14128.
[20] T. Kick, J.H. Starcke, C. Naumann, Green propellant substituting hydrazine: investigation of ignition delay time and laminar flame speed of ethene/dinitrogen oxide mixtures, Proc. Eur. Combus. Meet. 2017 (2017).
[21] M. Yang, Y. Yang, C. Liao, C. Tang, C. Zhou, Z. Huang, The auto-ignition boundary of ethylene/nitrous oxide as a promising monopropellant, Combust. Flame 221 (2020) 64–73.

[22] W. Wang, H. Zhang, Laminar burning velocities of C2H4/N2O flames: experimental study and its chemical kinetics mechanism, Combust. Flame 202 (2019) 362–375.

[23] R. Mével, J.E. Shepherd, Ignition delay-time behind reflected shock waves of small hydrocarbons–nitrous oxide(–oxygen) mixtures, Shock Waves 25 (3) (2014) 217–229.

[24] S.T. Darian, M. Vanpee, A spectroscopic study of the premixed acetylene nitrous oxide flame, Combust. Flame 70 (1) (1987) 65–77.

[25] K.M. Aldous, B.W. Bailey, J.M. Rankin, Burning velocity of the premixed nitrous-oxide/acetylene flame and its influence on burner design, Anal. Chem. 44 (1) (1972) 191–194.

[26] K.K. Yalamanchi, X. Bai, N.D. Fernando, A.S. Lua, S. Cheng, Y. Li, C.-W. Zhou, S. S. Goldsborough, S.M. Sarathy, From electronic structure to model application of key reactions for gasoline/alcohol combustion: hydrogen-atom abstractions by CH3Ȯ radical, Combust. Flame 252 (2023) 112742.

[27] C. Yang, J.-T. Chen, X. Zhu, X. Bai, Y. Li, K.K. Yalamanchi, S.M. Sarathy, S. S. Goldsborough, S. Cheng, H.J. Curran, From electronic structure to model application of key reactions for gasoline/alcohol combustion: hydrogen-atom abstraction by CH3OȮ radicals, Proc. Combust. Inst. 39 (2023) 415–423.

[28] R. Tang, Y. Han, H. Chen, B. Qu, Y. Li, Z. Lu, Z. Xing, S. Cheng, Theoretical study of H-atom abstraction by CH3OȮ radicals from aldehydes and alcohols: ab initio and comprehensive kinetic modeling, Combust. Flame 259 (2024) 113175.

[29] D.H. Ess, K.N. Houk, Activation energies of pericyclic reactions: performance of DFT, MP2, and CBS-QB3 methods for the prediction of activation barriers and reaction energetics of 1,3-dipolar cycloadditions, and revised activation enthalpies for a standard set of hydrocarbon pericyclic reactions, J. Phys. Chem. A 109 (2005) 9542–9553.

[30] S. Grimme, C. Mück-Lichtenfeld, E.-U. Würthwein, A.W. Ehlers, T.P.M. Goumans, T.P.M. Lammertsma, Consistent theoretical description of 1,3-dipolar cycloaddition reactions, J. Phys. Chem. A 110 (2006) 2583–2586.

[31] Y. Li, R. Jiang, S. Xu, X. Gong, Theoretical study on the gas-phase oxidation mechanism of ethylene by nitrous oxide, propellants explos, Propellants Explos. Pyrotech. 47 (2022) e202200082.

[32] V. Parmon, G. Panov, A. Uriarte, A. Noskov, Nitrous oxide in oxidation chemistry and catalysis: application and production, Catal. Today 100 (2005) 115–131.

[33] Y. Liu, J. Li, Quantitative dynamics of the N2O + C2H2 = oxadiazole reaction: a model for 1,3-dipolar cycloadditions, ACS Omega 5 (2020) 23343–23350.

[34] F. Karami, M. Vahedpour, Theoretical study on the gas phase reaction mechanism of acetylene with nitrous oxide, Struct. Chem. 24 (2013) 1513–1526.

[35] H. Wu, R. Tang, Y. Dong, X. Ren, M. Wang, T. Zhang, S. Cheng, H atom abstractions from C1–C4 alcohols, aldehydes, and ethers by NO2: Ab initio and comprehensive kinetic modeling, J. Phys. Chem. A 129 (2025) 4724–4744.

[36] Z. Guo, H. Wu, R. Tang, X. Ren, T. Zhang, M. Wang, G. Liang, H. Guo, S. Cheng, Key kinetic interactions between NOX and unsaturated hydrocarbons: H atom abstraction from C3–C7 alkynes, dienes, and trienes by NO2, J. Phys. Chem. A 129 (2025) 2584–2597.

[37] H. Wu, R. Tang, X. Ren, M. Wang, G. Liang, H. Li, S. Cheng, Understanding key interactions between NOX and C2-C5 alkanes and alkenes: the ab initio kinetics and influences of H-atom abstractions by NO2, Combust. Flame 272 (2025).

[38] Y. Zhao, D.G. Truhlar, The M06 suite of density functionals for main group thermochemistry, thermochemical kinetics, noncovalent interactions, excited states, and transition elements: two new functionals and systematic testing of four M06-class functionals and 12 other functionals, Theor. Chem. Acc. 120 (2008) 215–241.

[39] A.D. McLean, G.S. Chandler, Contracted gaussian basis sets for molecular calculations. I. second row atoms, Z= 11–18, J. Chem. Phys. 72 (1980) 5639–5648.

[40] W.J. Hehre, R. Ditchfield, J.A. Pople, Self—Consistent molecular orbital methods. XII. Further extensions of gaussian—type basis sets for use in molecular orbital studies of organic molecules, J. Chem. Phys. 56 (1972) 2257–2261.

[41] M.P. Andersson, P. Uvdal, New scale factors for harmonic vibrational frequencies using the B3LYP density functional method with the triple-ζ basis set 6-311+ G (d, p), J. Phys. Chem. A 109 (2005) 2937–2941.

[42] R.A. Kendall, T.H. Dunning Jr, R.J. Harrison, Electron affinities of the first-row atoms revisited. Systematic basis sets and wave functions, J. Chem. Phys. 96 (1992) 6796–6806.

[43] S. Andrade, L.C. Gonçalves, F.E. Jorge, Scaling factors for fundamental vibrational frequencies and zero-point energies obtained from HF, MP2, and DFT/DZP and TZP harmonic frequencies, J. Mol. Struct. 864 (2008) 20–25.

[44] K.K. Irikura, R.D. Johnson, R.N. Kacker, R. Kessel, Uncertainties in scaling factors for ab initio vibrational zero-point energies, J. Chem. Phys. 130 (2009).

[45] J.M. Martin, Ab initio total atomization energies of small molecules—Towards the basis set limit, Chem. Phys. Lett. 259 (1996) 669–678.

[46] T.H. Dunning Jr, Gaussian basis sets for use in correlated molecular calculations. I. The atoms boron through neon and hydrogen, J. Chem. Phys. 90 (1989) 1007–1023.

[47] P. Zhang, S.J. Klippenstein, C.K. Law, Ab initio kinetics for the decomposition of hydroxybutyl and butoxy radicals of n-butanol, J. Phys. Chem. A 117 (2013) 1890–1906.

[48] T.J. Lee, J.E. Rice, G.E. Scuseria, H.F. Schaefer III, Theoretical investigations of molecules composed only of fluorine, oxygen and nitrogen: determination of the equilibrium structures of FOOF, (NO) 2 and FNNF and the transition state structure for FNNF cis-trans isomerization, Theor. Chim. Acta 75 (1989) 81–98.

[49] W. Collins, S. Hochgreb, N. Swaminathan, J. Chen, Simulation of NOx formation in dilute H2/CO/N2–air diffusion flames using full and reduced kinetics, in: Proc. Eur. Combus. Meet, 2007. Available at: http://www.me.berkeley.edu/gri_mech/.

[50] F. Neese, ORCA 5.0.4, A Quantum Chemical Program Package, Max Planck Institute for Chemical Energy Conversion, Mülheim an der Ruhr, Germany, 2023. Available at: https://orcaforum.kofo.mpg.de.

[51] M.J. Frisch, G. Trucks, H.B. Schlegel, G. Scuseria, M. Robb, J. Cheeseman, G. Scalmani, V. Barone, G. Petersson, H. Nakatsuji, Gaussian 16, Gaussian, Inc, Wallingford, CT, 2016. Available at: https://gaussian.com.

[52] Y. Georgievskii, J.A. Miller, M.P. Burke, S.J. Klippenstein, Reformulation and solution of the master equation for multiple-well chemical reactions, J. Phys. Chem. A 117 (2013) 12146–12154.

[53] J.A. Miller, S.J. Klippenstein, Master equation methods in gas phase chemical kinetics, J. Phys. Chem. A 110 (2006) 10528–10544.

[54] Y. Georgievskii, S.J. Klippenstein, Strange kinetics of the C2H6+ CN reaction explained, J. Phys. Chem. A 111 (2007) 3802–3811.

[55] C. Eckart, The penetration of a potential barrier by electrons, Phys. Rev. 35 (1930) 1303.

[56] C. Zhou, Y. Li, U. Burke, C. Banyon, K.P. Somers, S. Ding, S. Khan, J.W. Hargis, T. Sikes, O. Mathieu, An experimental and chemical kinetic modeling study of 1, 3-butadiene combustion: ignition delay time and laminar flame speed measurements, Combust. Flame 197 (2018) 423–438.

[57] W. Collins, S. Hochgreb, N. Swaminathan, J. Chen, Simulation of NOx formation in dilute H2/CO/N2–air diffusion flames using full and reduced kinetics, in: Proceedings of the European Combustion Meeting, 2007. Available at: http://www.me.berkeley.edu/gri_mech/.

[58] Y. Wu, S. Panigrahy, A.B. Sahu, C. Bariki, J. Beeckmann, J. Liang, A.A. Mohamed, S. Dong, C. Tang, H. Pitsch, Understanding the antagonistic effect of methanol as a component in surrogate fuel models: A case study of methanol/n-heptane mixtures, Combust. Flame 226 (2021) 229–242.

[59] P. Glarborg, J.A. Miller, B. Ruscic, S.J. Klippenstein, Modeling nitrogen chemistry in combustion, Prog. Energy Combust. Sci. 67 (2018) 31–68.

[60] H. Hashemi, J.M. Christensen, S. Gersen, H. Levinsky, S.J. Klippenstein, P. Glarborg, High-pressure oxidation of methane, Combust. Flame 172 (2016) 349–364.

[61] H. Hashemi, J.G. Jacobsen, C.T. Rasmussen, J.M. Christensen, P. Glarborg, S. Gersen, M. van Essen, H.B. Levinsky, S.J. Klippenstein, High-pressure oxidation of ethane, Combust. Flame 182 (2017) 150–166.

[62] J. Gimenez-Lopez, C.T. Rasmussen, H. Hashemi, M.U. Alzueta, Y. Gao, P. Marshall, C.F. Goldsmith, P. Glarborg, Experimental and kinetic modeling study of C2H2 oxidation at high pressure, Int. J. Chem. Kinet. 48 (2016) 724–738.

[63] M. Liu, M. Chen, R. Fan, Y. Liao, J. Wang, C.W. Zhou, Z.Y. Tian, Combustion kinetics of amines: exploring hydrogen atom abstraction reactions from primary amines by ṄH2 radicals, Proc. Combust. Inst. 41 (2025) 105832.

[64] T. Methling, M. Braun-Unkhoff, U. Riedel, An optimised chemical kinetic model for the combustion of fuel mixtures of Syngas and natural gas, Fuel 262 (2020) 116611.

[65] S.S. Nagaraja, J. Liang, S. Dong, S. Panigrahy, A.B. Sahu, G. Kukkadapu, W.J. Pitz, H.J. Curran, A hierarchical single-pulse shock tube pyrolysis study of C2-C6 1-alkenes, Combust. Flame 219 (2020) 456–466.

[66] S. Dong, K. Zhang, P.K. Senecal, G. Kukkadapu, S.W. Wagnon, S. Barrett, N. Lokachari, S. Panigaphy, W.J. Pitz, H.J. Curran, A comparative reactivity study of 1-alkene fuels from ethylene to 1-heptene, Proc. Combust. Inst. 38 (2021) 611–619.

[67] S. Panigrahy, J. Liang, S.S. Nagaraja, Z. Zuo, G. Kim, S. Dong, G. Kukkadapu, W. J. Pitz, S.S. Vasu, H.J. Curran, A comprehensive experimental and improved kinetic modeling study on the pyrolysis and oxidation of propyne, Proc. Combust. Inst. 38 (2021) 479–488.

[68] W. Yuan, L. Ruwe, S. Schwarz, C. Cao, J. Yang, O. Deutschmann, K. Kohse-Höinghaus, F. Qi, Insights into the interaction kinetics between propene and NOx at moderate temperatures with experimental and modeling methods, Proc. Combust. Inst. 38 (2021) 795–803.

[69] M.J. McNenly, R.A. Whitesides, D.L. Flowers, Faster solvers for large kinetic mechanisms using adaptive preconditioners, Proc. Combust. Inst. 35 (2015) 581–587.

[70] R. Sivaramakrishnan, M.-C. Su, J. Michael, S. Klippenstein, L. Harding, B. Ruscic, Rate constants for the thermal decomposition of ethanol and its bimolecular reactions with OH and D: reflected shock tube and theoretical studies, J. Phys. Chem. A 114 (2010) 9425–9439.

[71] L. Xing, S. Li, Z. Wang, B. Yang, S.J. Klippenstein, F. Zhang, Global uncertainty analysis for RRKM/master equation based kinetic predictions: A case study of ethanol decomposition, Combust. Flame 162 (2015) 3427–3436.

[72] S. Cheng, Y. Yang, M.J. Brear, M. Frenklach, Quantifying uncertainty in kinetic simulation of engine autoignition, Combust. Flame 216 (2020) 174–184.

[73] Q. Xu, B. Liu, W. Chen, T. Yu, Z. Zhang, C. Zhang, L. Wei, Z. Wang, Comprehensive study of the low-temperature oxidation chemistry by synchrotron photoionization mass spectrometry and gas chromatography, Combust. Flame 236 (2022) 111797.

[74] Y. Li, R. Jiang, S. Xu, X. Gong, Theoretical study on the gas-phase oxidation mechanism of ethylene by nitrous oxide, Propellants Explos. Pyrotech. 47 (2022) e202200082.

[75] G. Mittal, C-J. Sung, Aerodynamics inside a rapid compression machine, Combust. Flame 145 (2006) 160–180.

[76] G. Mittal, C-J. Sung, A rapid compression machine for chemical kinetics studies at elevated pressures and temperatures, Combust. Sci. Technol. 179 (2007) 497–530.

[77] C. Wadkar, P. Chinnathambi, E. Toulson, Analysis of rapid compression machine facility effects on the auto-ignition of ethanol, Fuel 264 (2020) 116–546.

[78] S. Cheng, D. Kang, A. Fridlyand, S.S. Goldsborough, C. Saggese, S. Wagnon, M. J. McNenly, M. Mehl, W.J. Pitz, D. Vuilleumier, Autoignition behavior of gasoline/

ethanol blends at engine-relevant conditions, Combust. Flame 216 (2020) 369–384.

[79] S. Cheng, C. Saggese, D. Kang, S.S. Goldsborough, S.W. Wagnon, G. Kukkadapu, K. Zhang, M. Mehl, W.J. Pitz, Autoignition and preliminary heat release of gasoline surrogates and their blends with ethanol at engine-relevant conditions: experiments and comprehensive kinetic modeling, Combust. Flame 228 (2021) 57–77.

[80] C. Yan, H. Zhao, Z. Wang, G. Song, Y. Lin, C.R. Mulvihill, A.W. Jasper, S. J. Klippenstein, Y. Ju, Low- and intermediate-temperature oxidation of dimethyl ether up to 100 atm in a supercritical pressure jet-stirred reactor, Combust. Flame 243 (2022) 112059.